

**Catalyst design concept based on a variety of alloy materials: a personal account and relevant studies**

Journal:	<i>Journal of Materials Chemistry A</i>
Manuscript ID	TA-PER-04-2020-003733.R2
Article Type:	Perspective
Date Submitted by the Author:	22-Jun-2020
Complete List of Authors:	Furukawa, Shinya; Hokkaido University, Institute for Catalysis Komatsu, Takayuki; Tokyo Inst Technol Shimizu, Ken-ichi; Hokkaido University, Catalysis Research Center

SCHOLARONE™
Manuscripts

Catalyst design concept based on a variety of alloy materials: a personal account and relevant studies

Shinya Furukawa^{*,†,‡,§} Takayuki Komatsu,^{||} Ken-ichi Shimizu,^{†,‡}

[†] *Institute for Catalysis, Hokkaido University, N-21, W-10, Sapporo 001-0021, Japan*

[‡] *Elements Strategy Initiative for Catalysts and Batteries, Kyoto University, Katsura, Kyoto 615-8520, Japan*

[§] *JST, PRESTO, 4-1-8 HonCho, Kawaguchi, Saitama, 332-0012, Japan*

^{||} *Department of Chemistry, School of Science, Tokyo Institute of Technology, 2-12-1-E1-10 Ookayama, Meguro-ku, Tokyo 152-8551, Japan*

Corresponding authors

Shinya Furukawa

Institute for Catalysis, Hokkaido University, N21, W10, Sapporo 001-0021, Japan

E-mail: furukawa@cat.hokudai.ac.jp,

Fax: +81-11-706-9162

Abstract

An overview of our recent advances in the development of highly efficient alloy materials for catalytic applications (intermetallic compounds, pseudo-binary, solid-solution, and single-atom alloys, and their derivatives) is provided as a personal account for the design of alloy-based catalysts. A series of important and emerging alloy materials and derivatives developed by other researchers for catalytic processes, such as Heusler alloys, high-entropy alloys, and rooted catalysts, are also introduced to cover a wide variety of such catalytic materials. The presented alloy materials are classified into (1) ordered, (2) disordered (random), and (3) precursors for nanocomposites, and each of them is further classified into subcategories based on their structure differences. The role of the metal elements, structural factors, and electronic properties in enhanced catalysis is also briefly explained by atomic scale interpretation.

Keywords: alloy; catalyst; intermetallic compound; pseudo-binary alloy; single-atom alloy; high-entropy alloy

1. Introduction

Metallic materials have been used as catalysts for a wide variety of molecular transformations in industrial, organic, pharmaceutical, and environmental chemistry.¹⁻³ The most favorable metal elements that show high catalytic activity toward the target reactions have been intrinsically determined. For instance, metals of group 8 (Ru, Fe, and Os) have been successfully applied for ammonia synthesis,⁴ Pt for the oxygen reduction reaction,⁵ Rh for the NO_x reduction,⁶ and Pd for various coupling reactions.⁷ The high performance of these metal was mainly due to their moderate interaction (adsorption affinity) with the reactant. In general, when a very weak interaction is developed, the adsorption to the catalyst is inhibited, whereas a very strong interaction prevents the product desorption from the catalyst. This trend is also known as the Sabatier principle.⁸ The catalytic properties of a pure metal element can be further modified by changing its electronic and/or geometric structure. For instance, the electronic state of the metal can be tuned using specific metal oxides as catalyst supports or co-catalysts.^{9, 10} For this conventional method, the effect of the additive is limited only to the interface between the metal nanoparticles and the oxide. Moreover, unmodified active sites distant from the metal–oxide interface are also present and often serve as less active or less selective reaction sites.¹¹

Alloying of the main active metal with a specific second metal has also been employed to modify the electronic and geometric structures.¹²⁻¹⁵ The active metal–metal ensembles can be diluted by the catalytically inert second metal, suppressing undesired side reactions such as C–C bond rupture (ensemble effect).¹⁶ In addition, the use of a second metal with different electronic properties than the main active metal, such as electronegativity or valence band structure, allows for a drastic change in the electronic structure due to the ligand effect.¹⁶ Moreover, the design of catalysts based on alloying allows the generation of homogeneously structured active sites. Provided that the desired alloy phase is formed with high phase purity, the structure of the active site is almost uniform and the number of modified active metal atoms can be maximized.

In order to prepare a well-designed multimetallic active site, the material should be designed based on the principles of metallurgy. Order studies in metallurgy have mainly focused on the physical properties of bulk alloys such as magnetism,^{17, 18} superconductivity,^{19, 20} shape memory effect,^{21, 22} and hydrogen storage capacity.^{23, 24} However, the chemical properties of the alloy's

surface, such as catalysis or adsorption, have rarely been investigated in this field. Therefore, a multidisciplinary approach to material design is required, which will be based not only on metallurgy and catalytic chemistry, but also on surface and computational science to construct a well-designed multimetallic active site for efficient molecular conversions.

To that end, we have developed a series of alloy catalysts with novel and unique surface structures that have been particularly efficient for challenging molecular transformations.²⁵⁻³³ As an overview of the catalyst design concept based on a variety of alloy materials, this paper outlines the fundamental aspect on different alloy types (section 2), the preparation and characterization of the desired alloy materials (section 3), and our recent progress in this field along with a brief introduction to emerging alloy-based materials developed by other researchers (sections 4–6). Moreover, this paper aims to clarify how widely and freely we can control and modify the structure and the resulting electronic or geometric properties by changing materials. For each topic, we provide a brief explanation for how the desired structure is designed and characterized, and why the catalytic performance is enhanced.

2. Classification and thermodynamics of alloys

In this paper, the alloy materials for catalytic use have been classified into three main categories, i.e., (1) ordered, (2) disordered (random), and (3) precursors for nanocomposite structures, presented in sections 4, 5, and 6, respectively. It has been proved that the atomic arrangement (ordered or not) depends strongly on the characteristics of the constituent metals.³⁴ In general, when the constituent metal elements are neighboring or very close to each other in the periodic table (i.e., they have similar electronic properties and atomic radii), the resulting alloy structure tends to be disordered. Instead, the combination of two or more metals that are distant in the periodic table leads to intermetallic compounds of ordered structures. The catalytically active zerovalent elements are mainly metal elements of the 8–11 groups (Fig. 1a).¹²⁻¹⁴ Therefore, random or ordered structures can be formed when the counterpart element combined with the main active metal belongs to the same or different class, respectively (Fig. 1b). Fig. 1c shows the phase diagram of a Pt–Pd bimetallic system³⁵ as a representative example of random alloys. Pt and Pd are miscible in any composition ratio and form a solid-solution alloy with random Pt–Pd distribution without altering the parent

face-centered cubic crystal structure. However, when the second metal is typical or early transition metal, different results are obtained. For instance, for the Pt–Sn system,³⁶ only a limited number of intermetallic phases are allowed with numerical composition ratios i.e., Pt₃Sn, PtSn, Pt₂Sn₃, PtSn₂, and PtSn₄ (Fig. 1d), while the solid-solution phase is allowed only for Sn poor ratios (Sn <10%). Moreover, the intermetallic phases have unique crystal structures with different space groups and atomic arrangements than those of the parent pure metals. An intermediate state is observed for moderately different metal elements such as Pt–M (M = Fe, Co, and Cu). This class exhibits a unique phase diagram as shown in Fig. 1e for the Fe–Pt system,³⁴ where both ordered (called as Kurnakov-type intermetallic compounds) and disordered structures are allowed depending on the temperature and composition ratio. Moreover, the ordered structure appears only at low-temperature regions within a limited composition range.

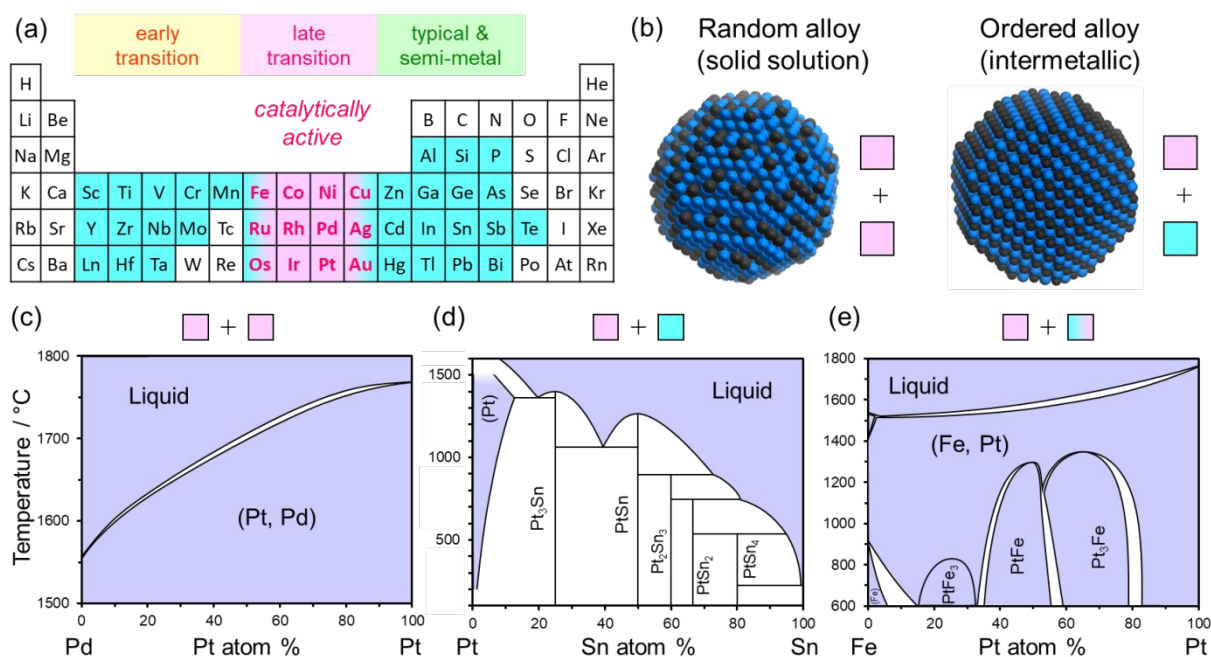


Fig. 1. (a) Classification of catalytically active or inert metal elements in the periodic table. (b) Structural models of nanoparticulate random and ordered alloys. Phase diagrams of (c) Pd–Pt,³⁵ (d) Pt–Sn,³⁶ and (e) Fe–Pt systems³⁴ reproduced from the database of National Institute for Materials Science (NIMS) AtomWork <<http://crystdb.nims.go.jp/>> with simplification for better visibility.

The observed trend in atom distribution can be explained by the formation enthalpy (ΔH_f) and entropy (ΔS_f) values for alloying using pure metals.¹⁶ When the properties of the constituent metals are very close, the ΔH_f value is close to zero or slightly negative (0–10 kJ/mol).¹⁶ Therefore, the

disordered structure ($\Delta S_f > 0$) is favored, so that a negative formation free energy is obtained ($\Delta G_f = \Delta H_f - T\Delta S_f$), whereas the ordered structure is unfavorable in terms of entropy. However, when the electronic properties of the metal constituents are particularly different, ΔH_f has a very negative value due to the significant charge re-distribution.³⁷ This sufficiently compensates for the entropy loss, resulting in a negative ΔG_f value. For Kurnakov-type intermetallic compounds, the disordering from the intermetallic to the solid-solution phase occurs when the temperature raises. This phase change can be attributed to the enhanced contribution of the entropy term at a high temperature region ($-T\Delta S_f$).¹⁶ Thus, it is clear that the driving formation forces of ordered (enthalpy-driven) and disordered (entropy-driven) alloys are completely different.

In this paper, ordered and disordered (random) alloys are further classified into subcategories with specific names, structures, and catalytic properties. The alloy materials that were used as starting materials to prepare more complex nanocomposites are also introduced. In addition, the catalyst design concept adopted in each subcategory and the individual development of efficient catalytic systems are also presented.

3. Preparation and characterization

Understanding the fundamental aspects of the preparation and characterization of the desired inorganic structures is essential for the design and synthesis of materials. In this section, we briefly introduce our strategy on the preparation of alloy materials and the standard characterization techniques used for the resulting materials. For the application of alloy materials in heterogeneous catalysis, these should be present in a nanoparticulate state grafted on an oxide- or carbon-based support with high surface area to achieve high metal dispersion (utilization efficiency) and catalytic activity. Solution synthesis methods using organic protecting agents have also been developed, leading to nanoalloys effective for heterogeneous catalytic systems in liquid phases.^{38, 39} However, for gas phase reactions, the organic agents remaining on the alloy surface hinder the access of reactant gases to the active site, typically resulting in poor catalytic performances. Thus, for the preparation of supported nanoalloys, we generally use conventional and/or advanced impregnation methods that do not require the addition of organic agents. Besides, we mainly use SiO_2 as the catalyst support due to its (1) high specific surface area ($>500 \text{ m}^2 \text{ g}^{-1}$), (2) poor anchoring ability,

and inertness in (3) chemical treatments and (4) catalytic reactions. These properties are favorable for high metal dispersion, better alloying, avoiding chemical transformation of the support itself, and understanding the roles of an alloy phase in catalysis, respectively. In contrast, strong anchoring ability, as observed for γ -Al₂O₃, often inhibits the reduction of metal precursors and the subsequent alloying,⁴⁰ requiring higher temperatures for a complete reduction and alloying during catalyst preparation. Furthermore, carbon-based supports cannot be used when calcination is involved in the preparation or regeneration process. The acid-base properties of some oxide supports may complicate the reaction mechanism or induce undesired side reactions, e.g., cracking caused by acidity. However, specific supports should be used when they own particular properties, such as acid-base properties^{41, 42} or surface hydroxyl groups²⁸, that provides some enhancement or concerted effect in catalysis. A conventional wet impregnation method using an excess amount of mixed aqueous solution of metal precursor salts has been applied for preparing alloy nanoparticles supported on oxides other than SiO₂ such as Al₂O₃, TiO₂, CeO₂, and MgO.^{40, 43} Instead, when the support is SiO₂ with large pore volume, a pore-filling impregnation method is applied,⁴³ where a minimum amount of the precursor solution is used just to fill the pore. In the absence of excess amount of water, the precursor condensation, which usually leads to inhomogeneous particle aggregation and alloying, can be suppressed during the subsequent drying process of the wet mixture. The homogeneous distribution of the precursor salts on the support surface is one of the most critical factors for determining the homogeneity of alloying. The precursor distribution is also differently affected by the charge of the metal precursor: whether the metal precursor complex is cationic (aquo or ammine), neutral (acetylacetonato or dinitrodiammine), or anionic (tetra- or hexachloro). Based on extensive studies on the support's isoelectric point for the preparation of heterogeneous catalysts,⁴⁴⁻⁴⁶ cations have proved to be favorable for acidic supports leading to better dispersion, whereas anions are beneficial for basic supports. The reduction and annealing process is another important factor for efficient alloying. When gaseous H₂ is used as the reductant, a high reduction temperature of 400–900°C is needed to reduce the metal precursors depending on their reduction potentials.⁴⁷ Under these high temperature conditions, the formed nanoparticles are also annealed so that the constituent metals are completely alloyed. However, reduction temperatures higher than 900°C are unfavorable for oxide supports due to the significant sintering and surface area

loss of the support. Liquid phase reduction (LPR) using borohydrides⁴⁸ or sodium naphthalenide⁴⁹ can also be used as an alternative reduction method performed at near room temperature. LPR at low temperature allows the formation of small nanoparticles without aggregation and the reduction of early transition metals such as Ti^{48, 49} or Zr,⁵⁰ which are hardly reduced by H₂ even at 900°C.

After their preparation, the obtained catalysts are initially characterized by lab-scale X-ray diffraction (XRD) analysis to briefly check the degree and homogeneity of alloying and the crystallite size. In the case of incomplete alloying or unexpected severe sintering, the improvement in the preparation conditions is explored. For alloy nanoparticles with sizes of <3 nm that cannot be successfully analyzed by lab-scale XRD (typically with Cu K α radiation at $\lambda = 1.54 \text{ \AA}$), synchrotron XRD using hard X-ray with much shorter wavelength (<0.5 \AA) can be used (section 4.2). A detailed characterization of the prepared catalyst can also be achieved by high-angle annual dark-field scanning transmission electron microscopy (HAADF–STEM) combined with energy-dispersive X-ray (EDX) analysis to observe alloy nanoparticles with specific atomic arrangement derived from the corresponding crystal structure, and identify the presence of each constituent element in the nanoparticles, respectively. We provide many examples of HAADF–STEM–EDX analysis in sections 4–6. Furthermore, for pseudo-binary alloys, the location of the third metal can be determined by X-ray adsorption fine structure (XAFS) analysis (section 4.2). Fourier-transform infrared (FT-IR) study with CO adsorption can be applied to characterize the nanoparticulate alloy surface. This technique provides information about the electron density and geometric state (diluted or isolated by second metals, section 5.2) of Pt-group metals on the surface of alloy nanoparticles. Besides, comparing experimental and theoretical (density functional theory (DFT)) data on CO stretching vibration allows to suggest the exposure of certain planes (section 4.1). In addition, X-ray photoelectron spectroscopy (XPS) is typically used to compare the surface electronic state of an alloy material and the corresponding pure metal. XPS analysis combined with Ar⁺ sputtering enables depth profiling, which is suitable for characterizing surface-modified intermetallics. Two representative examples are provided in section 6.1, where the modifier atoms are present only on the surface but not in the bulk. Thus, the combination of several characterization techniques mentioned above provides a deep insight into the feature and properties of the prepared nanoalloys, which, in its turn, allows a thorough understanding of the role of alloy phases in enhanced catalysis. In this paper,

various characterization results in each topic are introduced, which can strongly support the identification of crucial structural features.

4. Ordered alloys

4.1. Intermetallic compounds

Intermetallic compounds in catalysis are mainly characterized (1) by the drastic change in the electronic and geometric structures of the main active metal, which significantly improves the catalytic activity and selectivity compared to the corresponding monometallic catalyst, and (2) by a specific surface atomic arrangement with high regularity, which directly affects the adsorption conformation and surface dynamics of the reactant molecules, leading to high selectivity.

4.1.1. Drastic change in active site geometry

Monometallic catalysts consist of metal-metal ensembles that often trigger undesired side reactions such as the reactant or product fragmentation by C–C⁵¹⁻⁵⁴, C–O,^{55, 56} or C–N⁵⁷ cleavage. The active metal–metal ensembles are regularly diluted with inactive second metals when an intermetallic phase is formed. For example, many researchers including us have reported that intermetallic Pt₃M (M = Bi,⁵⁸ In,⁵⁹ Mn,⁶⁰ Sn,⁶¹⁻⁶⁵ etc.) phases show high alkene selectivity in alkane dehydrogenation. In this case, Pt is active not only for the C–H activation, but also for the C–C bond cleavage, while early transition and typical metals are almost catalytically inactive for these reactions. Especially for the C–C bond scission, large Pt–Pt ensembles of at least four atoms are required, so that the two fragmented C_xH_y species are stably captured.⁵⁴ Since the intermetallic Pt₃M phase has typically an L1₂ structure (space group: Pm $\bar{3}$ m), the most stable (111) surface displays a (2 × 2) structure consisting of Pt₃ ensembles and isolated M (the example for M = Sn is shown in Fig. 2).¹⁶

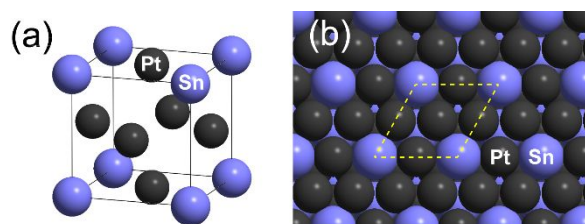


Fig. 2. (a) Crystal structure of Pt₃Sn with a single unit cell and (b) atomic arrangement of Pt₃Sn(111) surface with a (2 × 2)-Sn structure.

Therefore, the C–C bond cleavage that needs large Pt–Pt ensembles is effectively inhibited. Moreover, the adsorption of the alkene product also weakens, thus promoting the product desorption to improve selectivity.⁶¹ The decrease in the adsorption strength can be attributed to both electronic and geometric effects. Alloying of Pt with a p-block element significantly lowers the energy of the d band from the Fermi level,^{61, 66} which increases the occupation in the anti-bonding state of the surface Pt–C bond, thus weakening the bonding and molecular adsorption (electronic effect).^{67, 68} Besides, the dilution of large Pt–Pt ensembles disables the most stable adsorption configuration of unsaturated hydrocarbons,^{69, 70} which results in a less stable adsorption conformation and promotes desorption (geometric effect).

Similar catalyst design can be applied for the catalytic conversion of nitrogen-containing chemicals such as amines. Oxidative dehydrogenation of amines is a powerful synthetic tool to produce imines, which are important building blocks for various nitrogen-containing chemicals.⁷¹ However, during amine oxidation, undesired C–N scission often occurs and the imine selectivity decreases, because C–N bond is weaker than C–C bond. For example, the activation energy of benzylamine's C–N cleavage is 247 kJmol⁻¹,⁷² while that of ethylbenzene at the benzylic position is 264 kJmol⁻¹.⁷³ This trend is more prominent for amines of which N-atom bears a less bulky alkyl group (methyl or ethyl);⁷⁴ therefore, it remains challenging to selectively convert a wide variety of amines to the corresponding imines. Intermetallic Pd₃Pb, which has also a L1₂ structure like Pt₃Sn, serves as a selective catalyst for various amines, including primary, secondary, cyclic, benzylic, and aliphatic amines, with high imine selectivity.⁷⁴ For example, *N*-methyl- and *N*-ethyl-benzylamine have also been successfully converted to the corresponding imines with high yields. Besides, Pd₃Pb exhibits remarkably higher catalytic activity than monometallic Pd. Fig. 3a shows the time course of conversion during dibenzylamine oxidation with O₂ over Pd/MgO and Pd₃Pb/MgO catalysts.⁴² Pd/MgO showed a very low catalytic activity, reflecting the strong poisoning of the active Pd site by the product. As the imine product was strongly adsorbed on the Pd site, the reaction rate was limited by product desorption. However, Pd₃Pb/MgO exhibited particularly high catalytic activity, where a 180-fold higher turnover frequency (TOF) was obtained, and the reaction was completed within a few hours. In this case, the adsorption of imine was effectively weakened on the surface of Pd₃Pb

due to the electronic and geometric effect mentioned above, which significantly accelerated the rate-determining step, i.e., the imine desorption. In particular, the larger Pb atomic radius of Pb (Pd: 1.373 Å, Pb: 1.746 Å)⁷⁵ caused a large steric hindrance to the imine product and further promoted its desorption (Fig. 3b). An additional temperature-programmed desorption study of imine monitored by in-situ FT-IR technique demonstrated that the desorption of imine from Pd₃Pb occurred at a lower temperature than that from Pd.⁴²

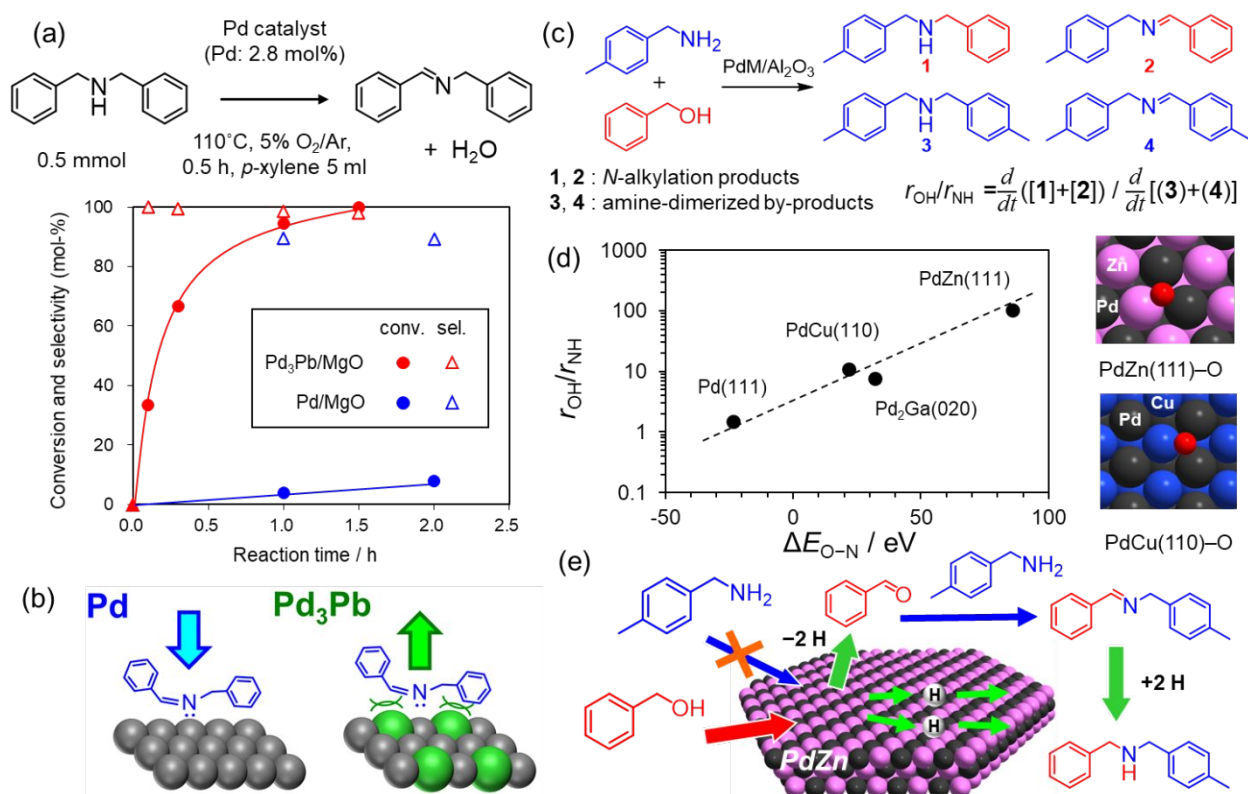


Fig. 3. (a) Aerobic oxidation of dibenzylamine over Pd₃Pb/MgO and Pd/MgO: reaction condition and time course of dibenzylamine conversion and *N*-benzylidenebenzylamine selectivity. (b) Schematic illustration of product imine desorption promoted by steric hindrance by large Pb atoms. (c) Reaction scheme of *N*-alkylation of 4-methylbenzylamine by benzyl alcohol using a Pd-based catalyst. (d) Relationship between the experimental selectivity for alcohol activation versus amine activation ($r_{\text{OH}}/r_{\text{NH}}$) and the difference in the adsorption energy of oxygen ($E_{\text{ad-O}}$) and nitrogen ($E_{\text{ad-N}}$) atoms on each surface ($\Delta E_{\text{O-N}}$). The figures on the right show examples of the slab models for the calculation of $E_{\text{ad-O}}$. (e) Reaction mechanism of selective *N*-alkylation of 4-methylbenzylamine over PdZn, where the alcohol is adsorbed on the surface and is activated more preferably than the amine.

We also introduce a different type of intermetallic surface, where the second metal is actively involved as an effective adsorption site for the reactant. The target reaction in this study was *N*-alkylation of amines using alcohols as alkylating agents, which is an important synthetic route to

secondary or tertiary amines.⁷⁶ Compared to other conventional *N*-alkylation methodologies, this reaction has many practical advantages such as mild reaction conditions and high atom efficiency. The reaction is initiated by dehydrogenation of alcohol, followed by the condensation of the generated carbonyl compound and the amine substrate to form *N*-alkylated imine and the subsequent hydrogenation of the imine to the *N*-alkylamine product.⁷⁷ Here, the hydrogen atom eliminated from alcohol is used for the final hydrogenation step, known as “hydrogen-borrowing” mechanism, which is mediated by a transition metal catalyst and indicates that no additional hydrogen source is required in contrast to reductive amination.⁷⁸ However, given that amines are generally more reactive than alcohols, the catalyst should activate the alcohol while keeping the amine intact. In particular, when the amine bears α -hydrogen(s), its undesired dehydrogenation to imine and the following condensation with a second amine (amine dimerization) occur as side reactions. A relevant example is given in Fig. 3c, where the reaction scheme of *N*-alkylation of 4-methylbenzylamine by benzyl alcohol is depicted. Compound **1** is the desired product, **2** is the intermediate imine, while **3** and **4** are the undesired by-products. The use of monometallic Pd/Al₂O₃ afforded **3** and **4** in the same amounts as **1** and **2**, where a formation rate ratio of 1.5 ($r_{\text{OH}}/r_{\text{NH}}$, corresponding to selectivity) was obtained. To avoid the undesired amine coupling, the investigation of this reaction was limited to amines that do not bear α -hydrogen atoms such as aniline and its derivatives. Nevertheless, the introduction of a second oxophilic metal promoted alcohol adsorption, helping to address this challenge. Fig. 3d shows the relationship between the experimental selectivity ($r_{\text{OH}}/r_{\text{NH}}$) to *N*-alkylation (alcohol activation) or amine dimerization (amine activation) for a series of Pd-based catalysts (Pd, PdCu, Pd₂Ga, and PdZn) and the adsorption energy difference of oxygen and nitrogen atoms ($\Delta E_{\text{O-N}}$) on these surfaces.⁴¹ For the Pd(111) surface, the adsorption of nitrogen atoms is preferred to that of oxygen atoms, indicating the intrinsic azophilic character of Pd. Therefore, both amines and alcohols were activated, resulting in a poor selectivity ($r_{\text{OH}}/r_{\text{NH}} \sim 1$). However, a reversed trend was observed for other Pd-based bimetallic surfaces. In particular, PdZn(110) showed a high $\Delta E_{\text{O-N}}$ value of 97 kJ/mol due to the strong oxophilic character of Zn. The *N*-alkylation selectivity linearly increased with increasing $\Delta E_{\text{O-N}}$, indicating that the oxophilic surface preferably captures alcoholic oxygen and inhibits the amine adsorption and the subsequent activation (Fig. 3e). Moreover, PdZn/Al₂O₃ exhibited excellent selectivity ($r_{\text{OH}}/r_{\text{NH}} = 104$) and yield (92%) for the desired *N*-alkylated product

when highly reactive benzylamine was used as a substrate. Thus, it was revealed that controlling the adsorption behavior of the reactant molecule plays a significant role in the catalytic performance especially when the molecule bears a heteroatom.

In summary, the changes in the geometric structure can drastically alter the catalytic properties. A similar effect, known as “ensemble effect”, could also be observed in random alloy structures.^{13, 14} However, ordered structures are superior to random structures in terms of regularity. Namely, the ordered structures always provide identical atomic arrangements, while different atom placements are observed for the random structures. For instance, the Pt₃Sn(111) intermetallic surface displays only Pt₃ trimers separated by isolated Sn atoms (Fig. 2b), whereas the Pt_{0.75}Pd_{0.25}(111) alloy surface has four distinct trimers (Pt₃, Pt₂Pd, PtPd₂, and Pd₃). The variety of surface structures may cause undesired side reactions that decrease selectivity. Therefore, bimetallic surfaces with high regularity are more suitable for selective molecular conversions.

4.1.2. Selective catalysis controlled by surface orderliness

In the last section, we suggested the advantages of ordered structures over random structures in selective catalysis. This is, however, not what only intermetallic compounds can do. In contrast, the specific surface atomic arrangement of some intermetallic compounds can be exploited to achieve highly challenging molecular transformations, such as chemo-, stereo-, and regio-selective hydrogenation. On such surfaces, the adsorption conformation and surface dynamics of the reactant molecules/atoms are sterically confined by two types of metal atoms that are aligned specifically and regularly. This steric restriction allows the highly selective molecular transformation, which may be what only intermetallic compounds can do and generally cannot be achieved by other inorganic materials including random alloys. In this section, we introduce three Rh-based intermetallic compounds with unique surface atomic arrangements of one-dimensionally aligned Rh arrays that can be successfully applied for selective hydrogenations.

The first example refers to the stereoselective isomerization of alkenes. Isomerization of *cis*- to *trans*-alkenes is generally hindered because the C=C bond cannot twist at the ground state. Therefore, protonation (acid-catalysis)⁷⁹ or photoexcitation⁸⁰ is conventionally employed to trigger the C–C bond rotation and the subsequent alkene isomerization. Neutral hydrogen atoms on a metal surface

can also catalyze the *cis-trans* alkene isomerization. According to the Horiuti–Polanyi mechanism established in 1930,⁸¹ the isomerization proceeds via a hydrogen attack on the alkenyl carbon, forming an alkyl intermediate. Then, the C–C bond rotates and a β -hydrogen elimination follows, resulting in the *trans*-isomer. However, the second hydrogen attack may occur, leading to a further hydrogenation that affords an alkane as the final product. Indeed, the isomerization occurs as a side reaction of alkene hydrogenation when transition metal catalysts are used, suggesting that the selective *cis-trans* isomerization of alkenes in the presence of H₂ is particularly challenging. Thus, the hydrogen attack on the alkenyl carbon should be strictly restricted to prevent the overhydrogenation of alkanes. We recently discovered that specific Rh- and Ru-based intermetallic compounds in the space group *Pnma* (RhSb, RhGe, and RuSb) can serve as an ideal platform for specific hydrogenation and selective isomerization.⁸² Figs. 4a and b show the unit cell of RhSb and its equilibrium crystal shape estimated by the Wulff construction.

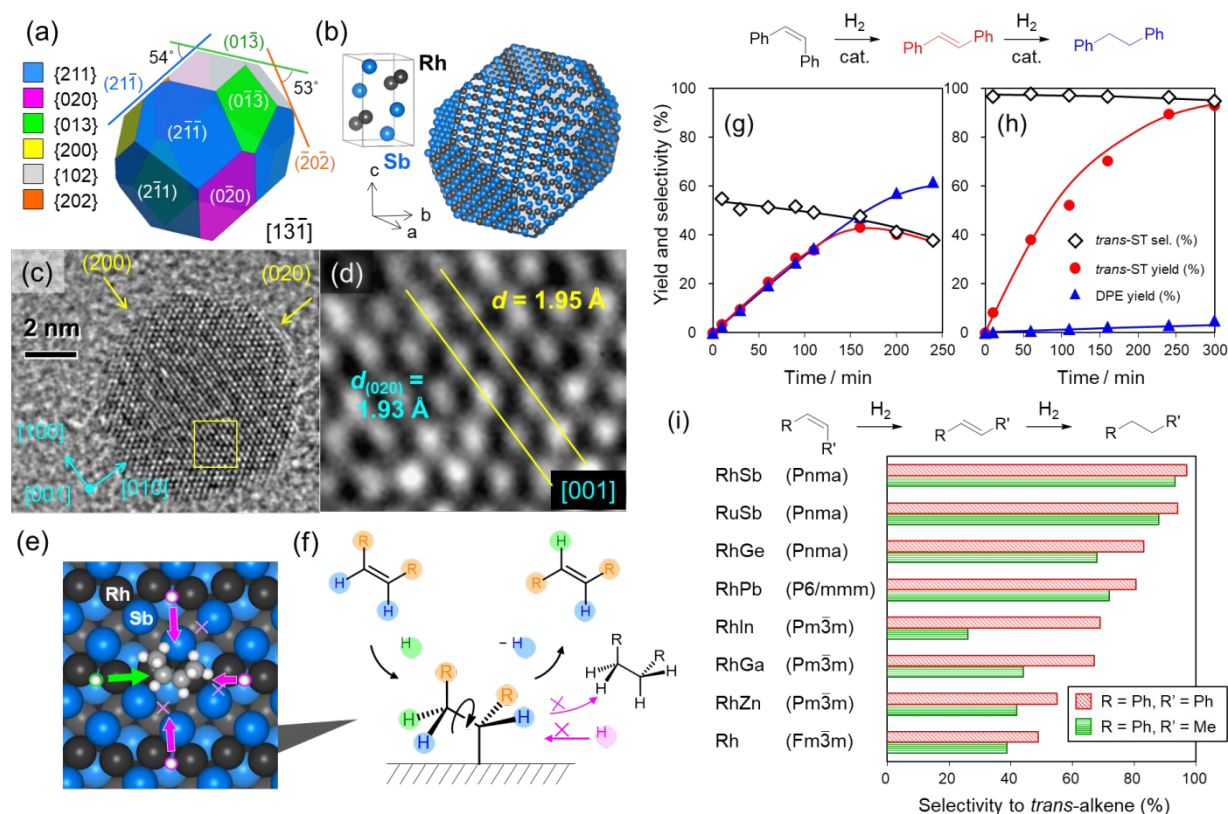


Fig. 4. (a) Equilibrium crystal shape of RhSb determined by the Wulff construction. (b) Crystal structure of RhSb: (left) single unit cell and (right) surface atomic arrangements displayed in (a). (c) high-resolution transition electron microscopy (HRTEM) image of a RhSb nanoparticle. (d) Enlargement of the yellow marked region in (c). (e) Geometric restriction of hydrogen access to *cis*-2-butene on RhSb(020). (f) Proposed mechanism of the selective *cis-trans*-alkene isomerization

without overhydrogenation to alkane. Time courses of *trans*-ST selectivity, *trans*-ST yield, and DPE yield in the liquid phase hydrogen-mediated isomerization of *cis*-ST over (g) Rh/SiO₂ and (h) RhSb/SiO₂. (i) Isomerization selectivities of *cis*-ST and *cis*-MS to the corresponding *trans*-alkenes catalyzed by various SiO₂-supported Rh- and Ru-based intermetallic compounds and monometallic Rh. The selectivities at 50% conversion are shown. The space group of each metallic phase is provided in brackets.

Most exposed surfaces have a unique atomic arrangement, i.e., one-dimensional zigzag Rh arrays separated by Sb. The high-resolution transition electron microscopy (HRTEM) images of the prepared RhSb/SiO₂ catalyst revealed that the nanoparticle is a single crystal of intermetallic RhSb and suggested a termination by the (020) and (200) planes (Figs. 4c and 4d). This termination was also supported by experimental and theoretical CO adsorption. In particular, the frequencies of the C=O stretching vibration on Rh obtained by IR spectroscopy agreed with those calculated by DFT for the (020), (013), and (211) surfaces, considering that the Sb-terminated (200) surface does not adsorb CO. Moreover, the alkene molecules and hydrogen atoms are very weakly adsorbed on Sb sites. Therefore, the alkene adsorption and hydrogen diffusion are allowed only on the Rh rows. A DFT calculation revealed that the energy barrier of hydrogen diffusion along the Rh row was 45 kJ mol⁻¹, while that across the Sb part was 200 kJ mol⁻¹, supporting the one-dimensional diffusion of hydrogen. We also calculated the adsorption state of the *cis*-alkene and the subsequent isomerization process. A unique adsorption geometry was observed (Fig. 4e), where only one alkenyl carbon was available for hydrogen attack, while the other was blocked by the connecting methyl moiety. The energy barrier of the hydrogen attack from the blocked side was higher than that from the open side, further confirming that the hydrogen attack on alkene is allowed only from one side and that a second hydrogen attack toward the alkane is sterically hindered (Fig. 4f). Thus, the specific and highly ordered surface structure can sufficiently control the adsorption geometry and the reaction dynamics. Figs. 4g and 4h show the catalytic performance of Rh/SiO₂ and RhSb/SiO₂ in the isomerization/hydrogenation of *cis*-stilbene (*cis*-ST). Although monometallic Rh/SiO₂ afforded diphenylethane (DPE) as the main product at high conversion regions, RhSb/SiO₂ catalyzed the selective isomerization to *trans*-stilbene in high yields. Maintaining high selectivity even at high conversion levels indicated that the hydrogenation of *trans*-alkenes to the corresponding alkanes can be effectively inhibited. What is interesting is that the isomerization selectivity depends strongly on

the space group of the metal catalyst, which, to the best of our knowledge, has never been reported before in heterogeneous catalysis. As shown in Fig. 4i, intermetallic compounds in the space group $Pnma$ (RhSb, RhGe, and RuSb) showed high *trans*-alkene selectivity, while those in cubic space groups ($Pm\bar{3}m$ and $Fm\bar{3}m$: RhIn, RhGa, RhZn, and Rh) exhibited poor selectivity. Although the $Pm\bar{3}m$ compounds (CsCl-type structure) have one-dimensional but straight Rh arrays on their stable (110) surface, they are not highly selective, probably because the zigzag surface structure of the $Pnma$ compounds is crucial for selectivity. Moreover, it should be noted that the selectivity also depends on the steric hindrance of the alkenyl carbons' alkyl substituents. Specifically, *cis*- β -methylstyrene (*cis*-MS) was slightly less selective for each catalyst than *cis*-ST due to the smaller steric hindrance caused by the methyl group in *cis*-MS compared to that caused by the phenyl moiety in *cis*-ST. As expected, the bulkier phenyl group more effectively hindered the second hydrogen attack on the alkenyl carbon, resulting in higher isomerization selectivity. Thus, intermetallic compounds with specific surface structures enable the stereoselective isomerization of *cis*-alkenes. This unique effect, which is mainly based on the specific surface atomic arrangement, can be called "alignment effect", which is truly what only intermetallic compounds can do.

The unique catalytic properties of intermetallic RhSb can be applied to more challenging and attractive reactions. Thus, we recently reported a tandem catalytic system of Pd₃Pb/SiO₂ and RhSb/SiO₂ for the selective hydrogenation of functionalized alkynes to (*E*)-alkenes.⁸³ The catalytic semihydrogenation of alkynes generally yields (*Z*)-alkenes as main products, while the corresponding (*E*)-alkenes can be hardly generated in high yields. Our tandem system enables the stepwise conversion of alkynes to (*Z*)- and (*E*)-alkenes over the Pd₃Pb/SiO₂ (semihydrogenation) and RhSb/SiO₂ (isomerization) catalysts, respectively. Both reactions are performed under H₂ at atmospheric pressure and room temperature, providing an efficient one-pot system under mild conditions. Another practical advantage of this system is its good functional group tolerance. The conventional isomerization protocols, such as acid-catalyzed or photoinduced reactions, usually trigger undesired side reactions on the alkyne functional groups. Instead, our system can be used for various alkynes bearing hydroxyl, carbonyl, carboxyl, and ester groups, affording the corresponding functionalized (*E*)-alkenes in high yields.

An additional representative example of this catalytic application is the molecular recognition for chemoselective hydrogenation of nitroarenes. Chemoselective hydrogenation of nitrostyrenes is an important process for the production of aminostyrenes, which are building blocks of polymers, dyes, and pharmaceuticals.^{84, 85} This reaction has been one of the hottest topics in the field of catalytic hydrogenation due to the difficult protection of the C=C moiety.⁸⁶ The hydrogenation of the C=C bond is kinetically and thermodynamically favored compared to that of the nitro (NO₂) group. Therefore, a specific modification of the reaction site is needed to protect the C=C bond from hydrogenation and selectively synthesize aminostyrenes in high yields. Thus, the adsorption mode of the C=C and NO₂ groups on the catalyst surface should be examined. When a 4-nitrostyrene (NS) molecule binds to the surface through the NO₂ group, the molecule stands vertically on the surface in a mono- or bidentate way via the lone pairs on the terminal oxygen of NO₂. In contrast, when NS interacts with the C=C group, the molecule lies on the surface via the π electrons projected vertically from the molecular plane. Therefore, the aromatic moiety is forced to bind to the surface in this adsorption fashion, in which a large metal–metal ensemble is required for strong adsorption. Thus, we tested a series of Rh-based SiO₂-supported intermetallic compounds (RhM/SiO₂; M = Bi, Fe, In, Pb, Sb, Sn, and Zn) for the hydrogenation of NS and deeply investigated the role of the surface structure on the selectivity.⁸⁷ Monometallic Rh/SiO₂ gave 4-ethylnitrobenzene (EN) as the main product, reflecting the difficulty of the selective hydrogenation using conventional monometallic catalysts. In contrast, Rh-based intermetallic catalysts afforded mainly 4-aminostyrene (AS) with varied selectivity (50–95%), depending strongly on the second metal. The highest selectivity (95%) was achieved when RhIn/SiO₂ was used, which also exhibited excellent catalytic performances for the hydrogenation of various nitroarenes bearing vinyl, formyl, acetoxy, ester, cyano, and halo groups. The corresponding aminoarenes were obtained in high yields (93–99%) within a few hours under an atmospheric pressure of H₂. A kinetic study further supported that the binding of the vinyl or nitro moiety to the metal surface significantly affected the selectivity. DFT calculations were also performed to clarify the adsorption energy of NS via vinyl and nitro moieties. Fig. 5 shows the relationship between the corresponding adsorption energies (E_{ad}) on the most stable surfaces of various Rh-based intermetallic compounds and the experimental selectivity of the Rh-based catalysts to NO₂ hydrogenation. The vinyl adsorption on the monometallic Rh(111) surface showed a negative

E_{ad} value due to the co-adsorption of the phenyl moiety. The aromatic C–H bond has an sp^3 -like conformation, which reflects the formation of a strong Rh–C bond on the surface. The E_{ad} value of the vinyl adsorption was more negative than that of the NO_2 adsorption. This indicates that vinyl adsorption and its hydrogenation is much more favorable and is consistent with the low NO_2 -hydrogenation selectivity. However, the vinyl adsorption was not favored on the Rh-based intermetallic surfaces with positive E_{ad} . This is partly because of the contribution of the ensemble effect: for instance, for RhZn(110), the multi-fold adsorption of the phenyl ring on the diluted Rh–Rh ensembles is inhibited by Zn. The conformation of the aromatic C–H bond turns to sp^2 -like, implying that the interaction between Rh and the phenyl ring is weak. However, the ensemble effect alone is not enough for the selective recognition of the NO_2 and vinyl groups. Fig. 5 also reveals that Rh-based intermetallic surfaces having second metals with larger atomic sizes than Rh such as In and Bi show high positive E_{ad} values for vinyl adsorption and high selectivity for NO_2 hydrogenation.

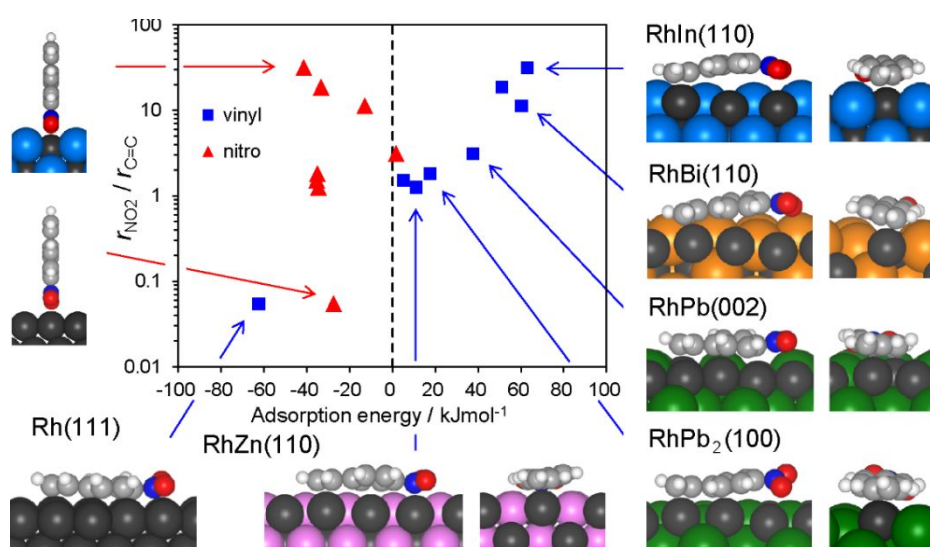


Fig. 5. Relationship between NO_2 -hydrogenation selectivity ($r_{\text{NO}_2}/r_{\text{C}=\text{C}}$) and adsorption energy of NS on slab models with vinyl (square) or nitro (triangle) moiety. NS structures interacting with Rh-based intermetallic compounds are shown around the graph.

On such a surface, the π plane of NS molecule should bend so that the vinyl moiety binds to the concave Rh row. This is attributed to the considerable steric hindrance of the convex In or Bi part. On the contrary, the NO_2 adsorption is allowed and gives negative E_{ad} values even on the concave Rh rows, because the end-on adsorption conformation fits within the concave Rh rows and is free of

the steric hindrance by the convex part. Thus, the RhIn surface is capable of distinguishing NO_2 adsorption with end-on coordination from vinyl adsorption with a side-on mode. We call this additional unique effect of intermetallic compounds as "steric effect".

Similar but more challenging molecular transformations can be achieved by exploiting the steric and alignment effects. The target reaction here is selective hydrogenation of dienes to monoenes. For instance, the conversion of 1,4-hexadiene to 2-hexene requires not only regioselectivity to distinguish the position of the C=C bond (terminal or inner), but also chemoselectivity to prevent the overhydrogenation of the product monoene to a saturated alkane. Given that an inner C=C moiety always has two or more alkyl groups on both sides, while no alkyl group is bound to the end of a terminal C=C bond, the difference in steric hindrance could be recognized on the surface of intermetallic compounds showing the steric effect. We discovered that intermetallic RhBi was suitable for this molecular conversion.⁸⁸ RhBi/SiO₂ exhibited a high 2-hexene selectivity (regioselectivity), which was maintained even for the complete conversion of 1,4-hexadiene (chemoselectivity), affording 2-hexene in 96% yield. Besides, various dienes, such as conjugated, unconjugated, branched, and cyclic dienes, can afford the corresponding inner alkenes in high yields using RhBi/SiO₂. Figs. 6a and 6b show the HAADF-STEM image of RhBi/SiO₂ and the elemental map of Rh and Bi. Small nanoparticles consisting of Rh and Bi with 3–5 nm size were homogeneously formed on the SiO₂ surface. The high-resolution image of a single nanoparticle indicated the presence of hexagonally aligned metal atoms, which agreed with the crystal structure of intermetallic RhBi (space group: $P6_3/mmc$) with the (110) termination observed along the [001] direction (Figs. 6c and 6d). Thus, intermetallic RhBi is formed as a nanoparticulate single crystal with a highly ordered structure. The termination by (110) planes was also confirmed by FTIR with CO adsorption and DFT calculations. The CO adsorption was simulated on the most stable (110) and the second stable (102) planes and the theoretical vibrational frequencies of CO were consistent with the experimental values (Fig. 6e). The adsorption behavior and hydrogenation process of 1,4-hexadiene was also investigated by DFT, as shown in Fig. 6f. The RhBi(110) surface also displayed one-dimensionally aligned Rh rows separated by zigzag Bi parts. The diene molecule lied along the Rh row, while the two C=C moieties were bound to the Rh atoms with di- π conformation.

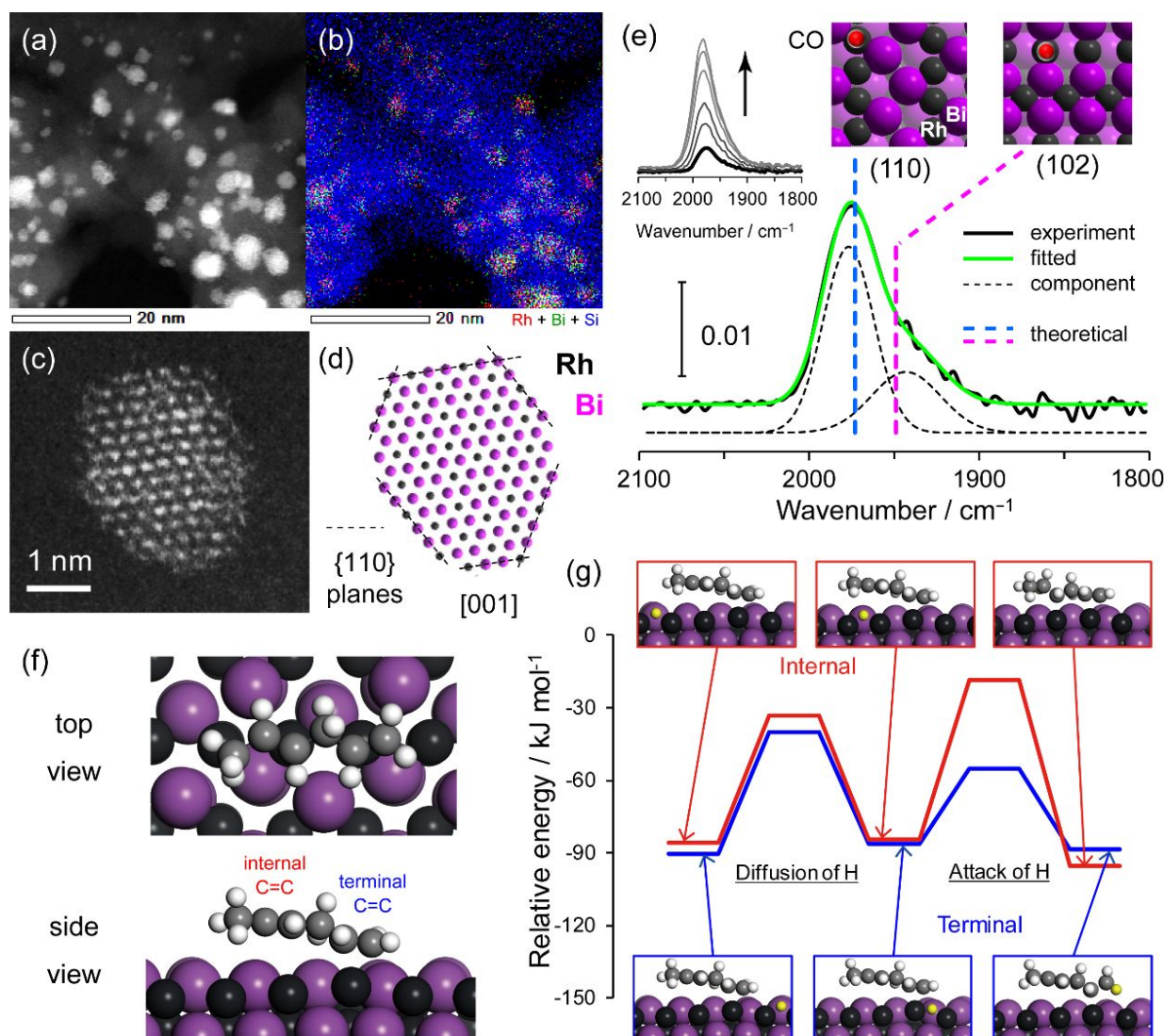


Fig. 6. (a) HAADF-STEM image of RhBi/SiO₂ and (b) corresponding elemental map of Rh (red), Bi (green), and Si (blue) acquired using EDX. (c) HR-STEM image of a single RhBi nanoparticle. (d) Crystal structure of intermetallic RhBi along the [001] direction as a structural model of (c). (e) FT-IR spectrum of CO adsorbed on RhBi/SiO₂. Bold dashed lines indicate the theoretical vibrational frequencies of CO adsorbed on the top sites of the (110) and (102) planes. The upper left inset shows the change in the FT-IR spectra with increasing CO pressure from 10 to 5000 Pa. (f) Optimized adsorption structure of 1,4-hexadiene on the RhBi(110) surface. (g) Energy diagrams for C=C hydrogenation of 1,4-hexadiene over the RhBi(110) surface. All energies are relative to 1,4-hexadiene in gas phase together with the slab with hydrogen.

Moreover, as hydrogen diffusion was restricted in the direction parallel to the Rh rows, a hydrogen attack on the alkenyl carbon was allowed only from the axial direction of the molecule. Besides, the inner C=C moiety was distant from the Rh row due to the steric hindrance between the large Bi atoms and the end methyl group. In addition, the energy barrier of hydrogen attack on the inner alkenyl carbon was found much higher than that on the terminal one (Fig. 6g), which demonstrates that the inner C=C moiety is protected for hydrogenation. This is also why the highly

chemoselectivity to inhibit overhydrogenation to alkane was observed. Thus, the combination of steric and alignment effects enables highly challenging molecular transformations.

In summary, some Rh-based intermetallic compounds have unique ordered surface structures with one-dimensionally aligned and/or sterically hindered active Rh sites. A high degree of orderliness and regularity at the atomic level are also observed for the solid surface, which has not been reported so far for other inorganic materials. However, the suggested chemistry is mainly supported by theoretical calculations and a few indirect experimental data such as CO adsorption. Thus, more convincing experimental findings, e.g., by using a single crystal clean surface with surface science techniques, are necessary to establish the role of steric and alignment effects of intermetallic compounds in catalytic chemistry.

4.2. Pseudo-binary alloys

Although intermetallic compounds for catalyst materials have several attractive and useful advantages, in some cases, they hinder the development of additional efficient catalytic systems, because the metal combination and composition ratio cannot be flexibly changed. For instance, there are only five intermetallic phases (Pt_3Sn , PtSn , Pt_2Sn_3 , PtSn_2 , and PtSn_4) in the Pt–Sn system (Fig. 1d), where the Pt/Sn ratio is fixed and cannot be tuned. In contrast, the composition ratio of disordered alloys can be randomly changed. Pseudo-binary alloys are promising inorganic materials that combine the advantages of both intermetallic compounds and random alloys. These materials are described as $A_m(\text{B}_{1-x}\text{C}_x)_n$ and are formed by replacing a part of B in the parent intermetallic A_mB_n by a third metal C without changing the crystal structure of A_mB_n . $A_m(\text{B}_{1-x}\text{C}_x)_n$ can also be considered as solid solutions of A_mB_n and A_mC_n with a $(1-x):x$ ratio. Moreover, although the system is ternary, it can be considered as a binary system with unique structure, explaining also its characterization as pseudo-binary material. Fig. 7 shows the phase diagram of a ternary Bi–Pb–Pt system⁸⁹ as a case study of trimetallic alloys. The linear lines observed between Pt_mPb_n and Pt_mBi_n indicate that Pb and Bi in $\text{Pt}_m\text{Pb}(\text{Bi})_n$ are miscible within the designated region. In particular, PtPb and PtBi are isomorphous, i.e., x in $\text{Pt}(\text{Pb}_{1-x}\text{Bi}_x)$ ranges between 0 and 1. In this review, we present two recent studies of our group on the development of pseudo-binary alloy catalysts for further improvement of the intermetallic compounds.

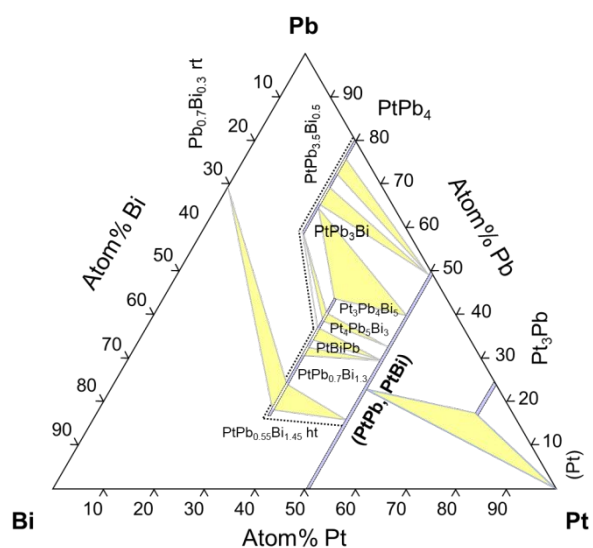


Fig. 7. Phase diagram of ternary Bi–Pb–Pt system at 200–900°C.⁸⁹ The diagram was reproduced from the database of National Institute for Materials Science (NIMS) AtomWork <http://crystdb.nims.go.jp/>

The first study focused on the NO reduction reaction using Pd-based materials. The NO-to-N₂ reduction is one of the key reactions in the purification of exhaust gases from automobiles,⁹⁰ where precious metals, such as Rh, Pt, and Pd, have long been used.^{91–94} One of the drawbacks of exhaust gas purification is the low N₂ selectivity at low temperatures (<250°C), where nitrous oxide (N₂O), a potent greenhouse gas, is largely formed as an undesired product.⁹¹ We recently observed that intermetallic PdIn supported on Al₂O₃ showed very high N₂ selectivity at low temperatures (100% selectivity at 200 °C) during the NO–CO reaction (Fig. 8a).⁹⁵ However, the catalytic activity of PdIn was much lower than that of monometallic Pd. Therefore, the catalytic activity of PdIn should be improved without impairing the N₂ selectivity. To that end, a new PdIn catalytic system was developed based on pseudo-binary alloys, by replacing a part of In by specific third metals (Figs. 8b and 8c). Among them, Cu was proved to be the best option as third metal element, as the NO conversion over Pd(In_{0.33}Cu_{0.67})/Al₂O₃ was significantly improved without lowering the N₂ selectivity. It should be emphasized that the catalytic performance of Pd(In_{1–x}Cu_x)/Al₂O₃ in the NO–CO reaction could be tuned depending on the Cu content. In particular, when the Cu content was low ($x = 0.33–0.5$), the improvement in the catalytic activity was not sufficient, suggesting that the PdIn-like character was not significantly affected. Instead, the N₂ selectivity decreased significantly in the presence of high Cu content ($x = 0.9$), indicating that the catalyst was converted to Pd-like and highlighting the need for a certain In amount to maintain high N₂ selectivity. Among the tested Cu

contents, the value of 0.67 provided the best performance with high NO conversion and N₂ selectivity.

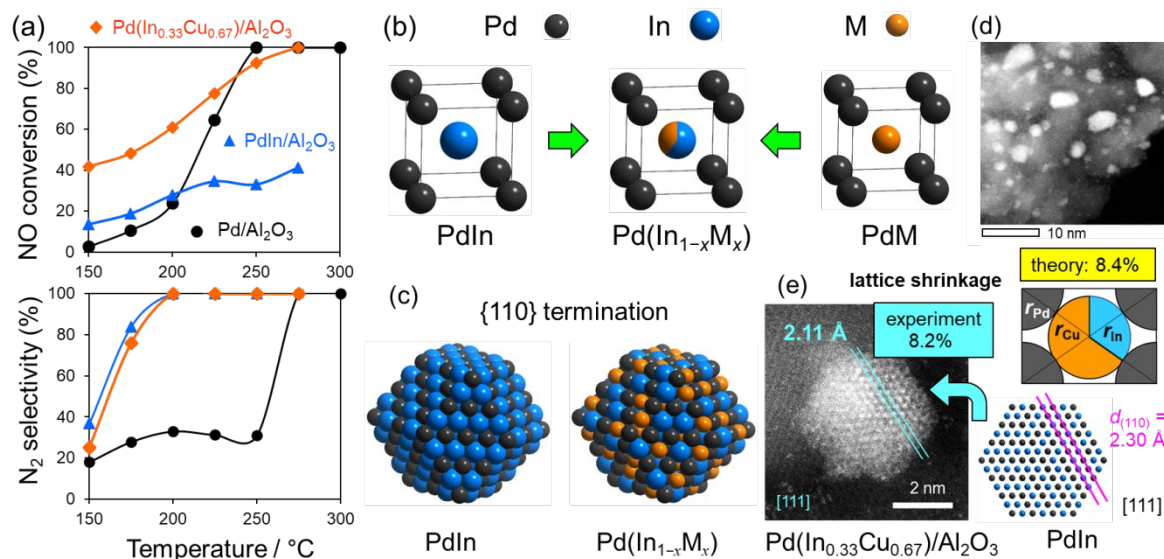


Fig 8. (a) NO conversion and N₂ selectivity during the NO–CO reaction over Pd-based catalysts. (b) PdIn-based pseudo-binary alloy with a CsCl-type structure obtained by substituting In by a third metal (M). (c) Models of nanoparticulate PdIn and Pd(In_{1-x}M_x) with a rhombohedral structure with the most stable {110} termination. (d) High-resolution HAADF–STEM image of Pd(In_{0.337}Cu_{0.67})/Al₂O₃. (e) (left) Magnification of a single nanoparticle, (right down) rhombohedral crystal of PdIn viewed along the [111] direction, and (right top) theoretical estimation of lattice shrinkage based on Vegard’s law and atomic radii.

The studies on pseudo-binary alloys require also multiple characterizations to identify whether the desired alloy phase is actually formed. The combination of XRD and HAADF–STEM–EDX analyses are needed to determine the formation of the corresponding ordered alloy phase and the involvement of the three metal elements. A similar approach has been employed to characterize the binary intermetallic compounds. Fig. 8d shows the HAADF–STEM image of Pd(In_{0.33}Cu_{0.67})/Al₂O₃, where nanoparticles with an average size of 3.3 nm were observed. The atomic arrangement shown in the high-resolution image was consistent with the CsCl-type crystal structure of PdIn observed along the [111] direction (Fig. 8e). However, the observed lattice fringes with 2.11 Å spacing were slightly shorter than the interplanar distance of the PdIn(110) planes (2.30 Å), suggesting the shrinkage of the PdIn crystal lattice due to the substitution of In by the much smaller Cu (Pd: 1.373 Å, In: 1.660 Å, Cu: 1.276 Å).⁷⁵ The theoretical lattice shrinkage based on Vegard’s law was 8.4% and was consistent with the experimental shrinkage of 8.2%. However, this approach is not sufficient

for the complete structural assignment of pseudo-binary alloys, because the position of the third metal atoms in the crystal structure remains unclear. Hence, extended X-ray adsorption fine structure (EXAFS) analysis was applied, as it provides information about metal–metal bonding and can be used to characterize pseudo-binary alloys. Based on the EXAFS curve-fitting, Pd–In (In–Pd) and Pd–Cu (Cu–Pd) scatterings were mainly observed, while our attempt to make a fitting with a Cu–In scattering resulted in a large R factor. These results indicated that Cu was present only at the In site and supported the formation of the Pd(In_{1-x}Cu_x) pseudo-binary alloy structure. In addition, DFT calculations focusing on the elemental steps of NO-to-N₂ reduction, such as the N–O cleavage and the N₂O decomposition, revealed the roles of In and Cu on the enhanced catalysis in NO–CO reaction. PdIn had a very low activation energy (E_a) of N₂O decomposition; 18.6 kJmol⁻¹ at the terrace of (110) and <0.1 kJmol⁻¹ at the step of (210), which is the origin of high N₂ selectivity. In contrast, the E_a value of the N–O dissociation on the PdIn surface was higher than that of Pd (100.2 kJ mol⁻¹ at the step of Pd (511) and 111.8 kJ mol⁻¹ at the step of PdIn (210)) and, therefore, consistent with the lower NO conversion of PdIn. Moreover, the substitution of an In part on the PdIn(210) surface by Cu reduced the E_a value of the N–O dissociation to the Pd(511) level, demonstrating that Cu recovered the catalytic activity. Thus, the combination of In and Cu can effectively enhance the N₂ selectivity and NO conversion.

The second example refers to alkane dehydrogenation using Pt-based materials.⁹⁶ Methylcyclohexane (MCH) has been used as a promising hydrogen carrier due to the high hydrogen content, low toxicity, and availability in existing petroleum infrastructures.^{97, 98} The dehydrogenation of MCH is an on-site chemical process for hydrogen production, where Pt-based catalysts are typically used.^{99, 100} However, for the long-term production of high-quality hydrogen at a high rate, the dehydrogenation catalytic system should be active, selective, and durable for a long time. Hence, undesired side reactions, such as the demethylation of toluene that generates benzene and methane, should be minimized to suppress the formation of coke, which deactivates the catalyst, and preserve a high carrier and hydrogen purity. Our strategy for developing an efficient catalytic system for MCH dehydrogenation was the stepwise optimization of the second and third metal elements. First, a series of intermetallic Pt₃M/SiO₂ catalysts (M = Fe, Co, Cu, Zn, Ga, In, Sn, and Pb) were prepared and tested in MCH dehydrogenation, with Pt₃Fe/SiO₂ exhibiting the highest catalytic activity and

durability. It should be noted that Pt_3Fe showed better performance than Pt_3Sn , which is a known selective catalyst for alkane dehydrogenation. A part of Fe in $\text{Pt}_3\text{Fe}/\text{SiO}_2$ was then replaced by a series of third metals to prepare $\text{Pt}_3(\text{Fe}_{0.75}\text{M}'_{0.25})/\text{SiO}_2$ catalysts ($\text{M}' = \text{Co}, \text{Ni}, \text{Cu}, \text{Zn}, \text{Ga}, \text{In}, \text{Sn}, \text{and Pb}$), which were examined in the same reaction. Among them, $\text{Pt}_3(\text{Fe}_{0.75}\text{Zn}_{0.25})/\text{SiO}_2$ gave the best catalytic performance, namely a 2.7-fold higher TOF, 99.6% toluene selectivity, 400 ppm methane, and almost no deactivation even at 400 °C for several hours (Figs. 9a and 9b).⁹⁶

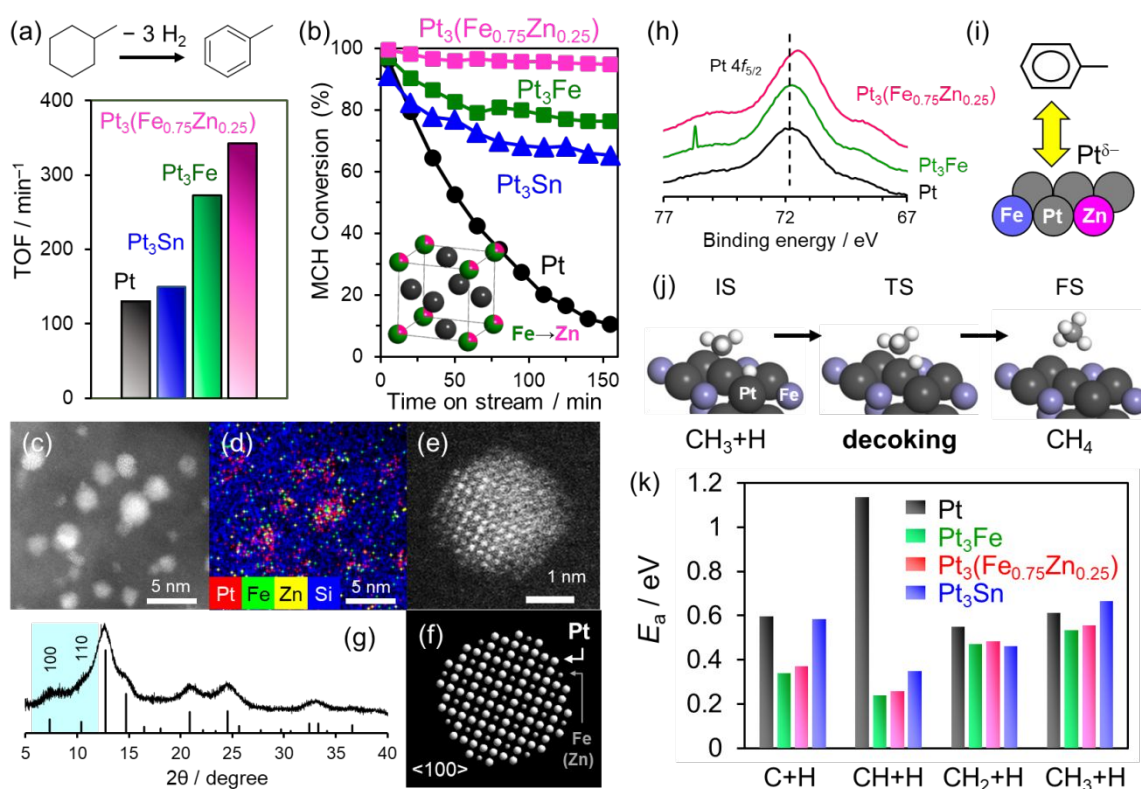


Fig. 9. Catalytic performance of SiO_2 -supported Pt-based catalysts in MCH dehydrogenation. (a) TOF at 300 °C and (b) change in MCH conversion during the durability test at 400 °C. (c) HAADF-STEM image of $\text{Pt}_3(\text{Fe}_{0.75}\text{Zn}_{0.25})/\text{SiO}_2$ and (d) corresponding elemental maps of the Pt/Fe/Zn overlayer obtained by EDX. (e) Magnification of the STEM image focusing on a single nanoparticle. (f) $\text{Pt}_3(\text{Fe}_{0.75}\text{Zn}_{0.25})$ crystal along the $\langle 001 \rangle$ direction (large: Pt, small: Fe or Zn). (g) Background-subtracted synchrotron XRD pattern of $\text{Pt}_3(\text{Fe}_{0.75}\text{Zn}_{0.25})/\text{SiO}_2$. The black vertical lines indicate the simulated diffraction patterns of $\text{Pt}_3(\text{Fe}_{0.75}\text{Zn}_{0.25})$. (h) Pt 4f XPS of Pt-based catalysts. (i) Schematic illustration representing the electrostatic repulsion between electron-rich Pt and toluene. (j) Initial (IS), transition (TS), and final (FS) states in CH_3 hydrogenation ($\text{CH}_3 + \text{H} \rightarrow \text{CH}_4$) on the $\text{Pt}_3\text{Fe}(111)$ surface. (k) Activation energy of CH_x (coke precursor) hydrogenation on $\text{Pt}_3\text{M}(111)$ calculated by DFT.

In addition, this catalyst exhibited the same catalytic performance (99% conv. and >99.8% sel.) for at least 50 h at 320 °C as a standard temperature in practical use. Multiple characterizations of

Pt₃(Fe_{0.75}Zn_{0.25})/SiO₂ confirmed the formation of the desired pseudo-binary alloy structure with the Fe–Zn substitution. HAADF–STEM–EDX analysis revealed that the nanoparticle had an intermetallic L1₂ structure and consisted of Pt, Fe, and Zn (Figs. 9c–f). The large difference in Z contrast allowed the differentiation of the dark Fe(Zn) columns and the surrounding bright Pt columns, which is consistent with the atomic arrangement of the L1₂ crystal structure observed along the <001> direction. The formation of the L1₂ structure was also confirmed by the synchrotron XRD pattern, which showed a superlattice diffraction of 100 and 110 characteristics to the L1₂ structure (Fig. 9g). EXAFS curve-fitting was also performed for the Pt-based catalysts (Table 1). For the Pt L_{III}-edge in Pt₃Fe, Pt–Pt and Pt–Fe scatterings could be distinguished with different coordination numbers and interatomic distances. The corresponding Fe–Pt scattering was also observed for Fe K-edge, while Pt₃(Fe_{0.75}Zn_{0.25})/SiO₂ gave similar results with the Pt–Pt, Pt–Fe(Zn), Pt–Pt, Fe–Pt, and Zn–Pt scatterings.

Table 1. Summary of the EXAFS curve-fitting for Pt-based catalysts.

sample	edge	shell	CN	R (Å)	σ^2 (Å ²)	R -factor (R^2)
Pt foil	Pt L _{III}	Pt–Pt	12.0 (fix)	2.77 ± 0.00	0.005	0.000
Pt/SiO ₂	Pt L _{III}	Pt–Pt	7.1 ± 0.3	2.73 ± 0.01	0.007	0.001
Pt ₃ Fe/SiO ₂	Pt L _{III}	Pt–Fe	2.0 ± 0.6	2.67 ± 0.02	0.014	0.003
		Pt–Pt	5.9 ± 0.5	2.71 ± 0.00	0.007	
	Fe K	Fe–O	0.8 ± 0.5	1.93 ± 0.02	0.006	0.008
	Fe–Pt	6.0 ± 1.1	2.64 ± 0.01	0.012		
Pt ₃ (Fe _{0.75} Zn _{0.25})/SiO ₂	Pt L _{III}	Pt–Fe	2.5 ± 0.7	2.66 ± 0.01	0.017	0.002
		Pt–Pt	5.8 ± 0.4	2.71 ± 0.00	0.007	
	Fe K	Fe–O	0.7 ± 0.7	1.92 ± 0.04	0.006	0.015
		Fe–Pt	7.6 ± 1.9	2.65 ± 0.01	0.013	
	Zn K	Zn–O	1.1 ± 1.1	2.01 ± 0.02	0.009	0.024
	Zn–Pt	6.8 ± 1.8	2.61 ± 0.02	0.019		

Our attempt to fit with Fe–Zn scattering resulted in a large R factor, suggesting little contribution of Fe–Zn bonds. Thus, we concluded that Zn was present at the Fe position in Pt₃Fe and that the desired pseudo-binary alloy structure was formed with Fe–Zn substitution.

A mechanistic study based on DFT calculations and XPS analysis was also performed to reveal the role of Fe and Zn on the enhanced selectivity and durability. The conventional ensemble effect i.e., the dilution of Pt–Pt ensembles by Fe and Zn, significantly weakened the toluene adsorption and promoted its desorption. The ligand effect was also provided by Zn, as the electron density of Pt

increased after alloying with Zn, which in turn enhanced the toluene electrostatic repulsion and desorption (Figs. 9h and 9i). Thus, the undesired side reactions of toluene were suppressed, and the selectivity was greatly improved. Besides, Fe was proved to play a unique role in the catalyst durability due to its contribution to decoking. In our study, we considered a stepwise hydrogen attack to a surface carbon atom to release methane ($\text{CH}_x + \text{H} \rightarrow \text{CH}_{x+1}$, $x = 0-3$) (Fig. 9j for $x = 3$) as a simple model of coke precursors removal. Fig. 9k depicts the E_a values of CH_x hydrogenation on $\text{Pt}_3\text{M}(111)$ surfaces. Fe-containing catalysts showed lower E_a than Pt and Pt_3Sn for each step, indicating that the surface Fe can promote the hydrogenation of coke precursors. Indeed, temperature-programmed oxidation of the used catalysts demonstrated that the amount of coke deposited on $\text{Pt}_3(\text{Fe}_{0.75}\text{Zn}_{0.25})/\text{SiO}_2$ was lower than that on other Pt-based catalysts. Thus, the combination of the ligand, ensemble, and decoking effects provided by Fe and Zn generates a highly active, selective, and durable catalyst for MCH dehydrogenation. Namely, the three metals elements involved in the pseudo-binary alloy that have individual effective functions (Pt: C–H activation, Fe: decoking, and Fe+Zn: desorption enhancement) can be adjacent at atomic level, allowing the preparation of a multifunctional, highly efficient active site for alkane dehydrogenation.

4.3. Heusler alloys

Heusler alloys, discovered by Heusler in 1903,¹⁰¹ are ternary intermetallic compounds with an L2_1 structure and an A_2BC chemical formula, where A represents late transition metals, B early transition metals and Zn, and C typical metals, as illustrated in Fig. 10a. Heusler alloys are particularly beneficial as catalyst materials, because a wide variety of constituent metals can be used, while the composition ratio and constituent metals can be easily tuned.¹⁰³ For instance, a part of metal B or C can be substituted by a fourth metal, B' or C', to form quaternary Heusler alloys with chemical formulas $\text{A}_2\text{B}(\text{C}_{1-x}\text{C}'_x)$ or $\text{A}_2(\text{B}_{1-x}\text{B}'_x)\text{C}$, respectively, which can be considered as "pseudo-ternary alloys" that allow for continuous tuning of the electronic factors without changing the crystal structure. The design of quaternary Heusler alloys is similar to that of pseudo-binary alloys (section 3.2), but it may be more flexible and widely applicable. Heusler alloys have been extensively studied in metallurgy for their physical properties such as spintronics,¹⁰⁴ thermoelectrics,¹⁰⁵ and shape

memory effects.¹⁰⁶ However, until recently, there were no reports on their application in catalysis, except for an early publication in 1935.¹⁰⁷

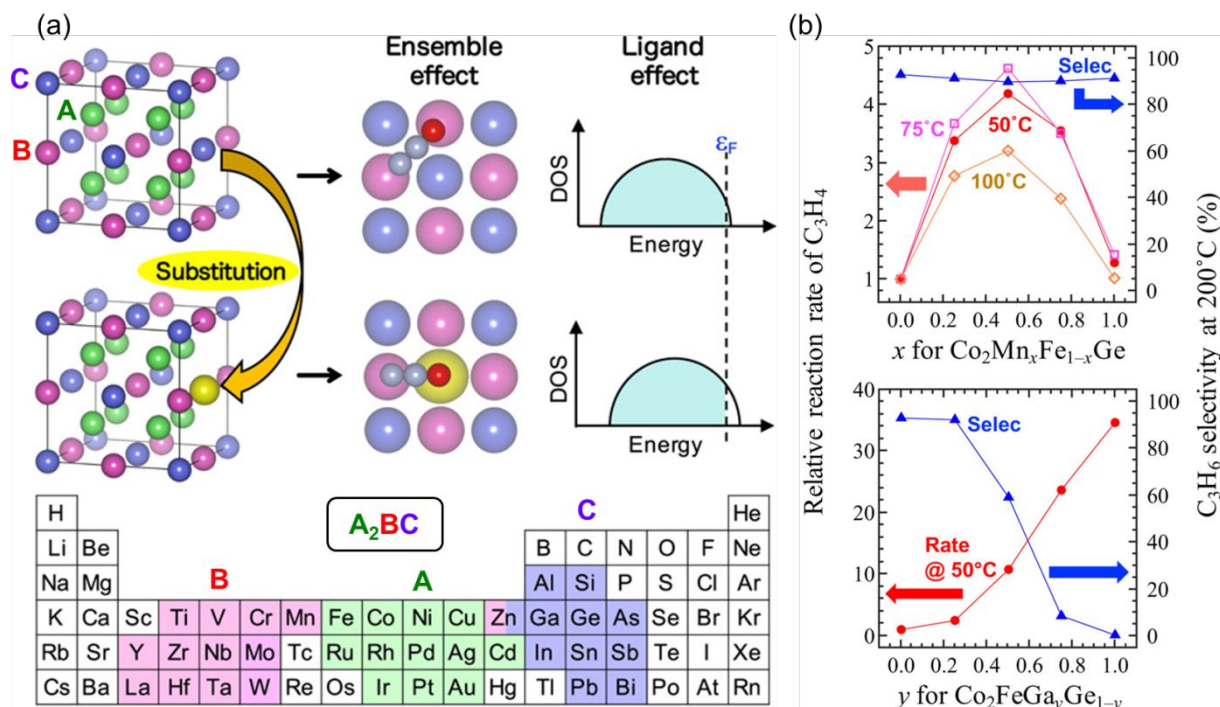


Fig. 10. (a) Schematic illustration of the effects of elemental substitution with the Heusler alloy's crystal structure (L2₁-type A₂BC). The typical elements used for A, B, and C are indicated in the periodic table. (b) Effect of elemental substitution on C₃H₄ hydrogenation. Change in the reaction rates of C₃H₄ per surface area and selectivities for C₃H₆ with variable (top) Mn (Co₂Mn_xFe_{1-x}Ge) and (bottom) Ga (Co₂FeGa_yGe_{1-y}) substitution. The blue triangles represent the selectivities for 100% C₃H₄ conversion at 200 °C. The reactant was a mixture of 0.1% C₃H₄/40% H₂/He balance. Reproduced with permission.¹⁰² Copyright 2018 American Association for the Advancement of Science.

Very recently, Kojima *et al.* reported a systematic study on the catalytic properties of 3d transition metal-based Heusler alloys (A = Fe, Co, Ni, and Cu) for alkyne semihydrogenation,^{102, 108} CO oxidation,¹⁰⁸ and methanol steam reforming.¹⁰⁹ For alkyne semihydrogenation, Co₂FeGe and the corresponding quaternary Heusler alloys with Fe–Mn and Ge–Ga substitution (Co₂(Fe_{1-x}Mn_x)Ge and Co₂Fe(Ge_{1-y}Ga_y), where $x, y = 0, 0.25, 0.5, 0.75,$ and 1) were tested. As shown in Fig. 10b, all the Co₂(Fe_{1-x}Mn_x)Ge catalysts exhibited high alkene selectivity (>90%), but the catalytic activity depended strongly on the Mn content, where a volcano-type dependence with a maximum at $x = 0.5$ was observed. However, the Co₂Fe(Ge_{1-y}Ga_y) series showed a different trend, as the catalytic activity increased monotonously and the selectivity decreased with increasing Ga content. Consequently, the

catalytic property can be successfully controlled by changing the metal components and the composition ratio. The increase in catalytic activity was explained by the ligand effect of Mn(Ga) and the d-band theory. Briefly speaking, when the d-band center is higher, the molecular adsorption is stronger and the energy barrier is lower. Indeed, the increase in x and y shifted the d-band center of the Heusler alloys to higher energies toward the Fermi level, and the apparent activation energy decreased linearly with the shift of the d-band center. In contrast, the decrease in catalytic activity in the presence of high Mn contents ($x > 0.5$) was explained by the enthalpy–entropy compensation effect. A stronger molecular adsorption (more negative ΔH) generally reduces the degree of freedom (lower ΔS) at the adsorbate state, which compensates for the contribution of the enthalpy and entropy terms in the Eyring-type equation that expresses the reaction rate. In that study, the decrease in the alkene selectivity by the Ge–Ga substitution was attributed to the adsorption of alkenes by Ga, which accelerated the overhydrogenation of alkene to the corresponding alkane. Thus, it was demonstrated that Heusler alloys are useful tools for tuning the catalytic performance and can be efficiently used as non-noble catalysts for selective alkyne semihydrogenation.

5. Random alloys

Random alloys are well-known materials and have long been investigated as catalytic materials. Their advantage is the wide solubility, which makes the catalyst design considerably flexible and tunable, leading to the formation of conventional one-to-one alloys or even single-atom alloys by changing the composition ratio. Besides, the number of constituent metals can be easily increased to form multimetallic solid-solution alloys such as high-entropy alloys.

5.1. Conventional solid-solution alloys

Solid-solution alloys formed between late transition metals (M_xN_{1-x} : $M = \text{Pt, Pd, Rh, etc.}$) have been extensively studied as catalyst materials and a number of papers have already published. Their history and achievements can be seen in the published reviews and books.¹¹⁰⁻¹¹³ A variety of metal elements that are fully or partially miscible with each other can be used for the preparation of such alloys. However, several combinations, e.g., Fe–Cu, Ni–Au, or Ru–Pd, have low or zero miscibility and cannot be alloyed by conventional preparation methods. Thus, specific approaches, such as

liquid phase reduction¹¹⁴⁻¹¹⁶ or double complex salts¹¹⁷⁻¹³² are needed to form the corresponding solid–solution nanoalloys. In this section, we present a part of our recent studies on catalysis using these materials.¹³³⁻¹³⁵ Our approach to develop efficient alloy catalysts is simple; the main metal, which is active for a specific reaction, is alloyed with various other metals (second metal survey) and their composition ratio is optimized. For bimetallic solid–solution alloys, their electronic states and catalytic performances can be flexibly tuned, since a wide range of composition ratios are available.

Fig. 11a depicts an application of Cu-based catalysis on heterogeneous alkene hydroboration. We recently found that Cu/Al₂O₃ can be used as a heterogeneous catalyst for the additive-free hydroboration of terminal alkenes in ethanol as the solvent.¹³³ However, the catalytic activity was very low for high product yields, which prompted us to develop a more efficient catalyst based on its alloying with other metals. The second metal survey and the following optimization revealed that alloying of Cu with a small amount of Ni improved the catalytic activity without affecting the product selectivity.¹³³

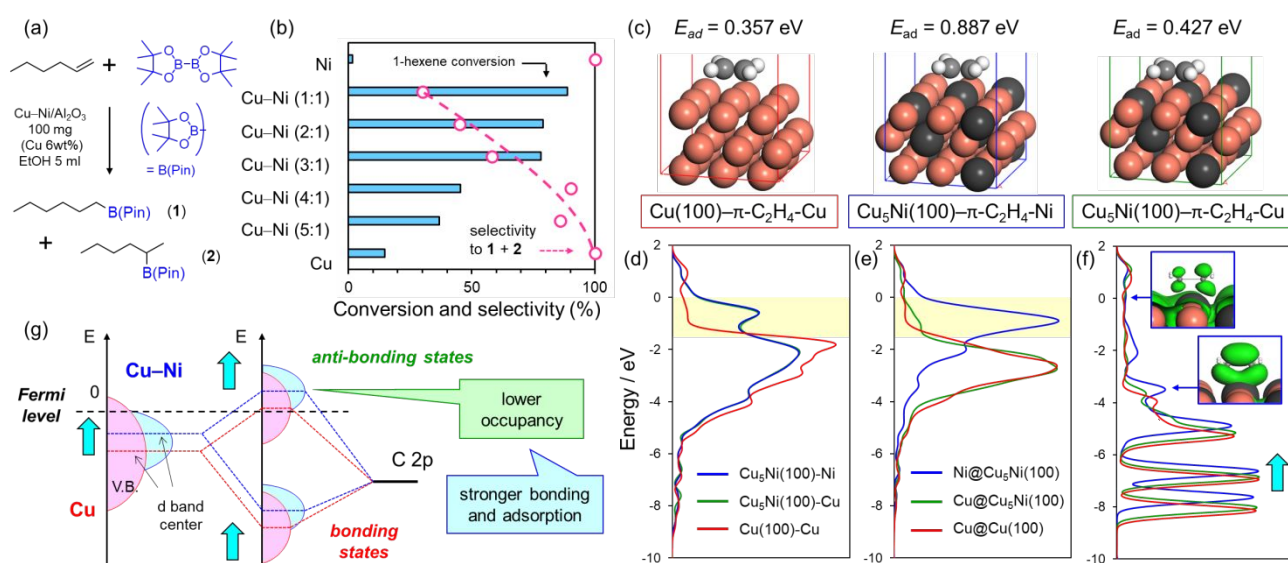


Fig. 11. (a) Reaction scheme and conditions of 1-hexene hydroboration. (b) Catalytic performance of Cu/Al₂O₃, Cu-Ni/Al₂O₃ (Cu/Ni = 1–5), and Ni/Al₂O₃, prepared by a deposition/precipitation method, in hydroboration of 1-hexene in 1 h. (c) Optimized ethylene structures adsorbed on Cu(100) and Cu-Ni(100) (Cu/Ni = 5) surfaces with a π -configuration. Ethylene can be adsorbed on both Cu and Ni atoms of Cu-Ni(100). (d) Total and local density of state (DOS) on (e) metal atoms adsorbing ethylene and (f) carbon atoms of ethylene. The insets show the orbitals of the states designated by blue arrows. (g) Schematic representation of the adsorption properties of alkene based on the d-band theory.

The results of the Cu–Ni ratio optimization with respect to the catalytic activity and selectivity are shown in Fig. 11b. The catalytic activity (1-hexene conversion) increased monotonously with the Ni content, whereas the selectivity to the desired boron-adduct decreased with higher Ni content due to the formation of *n*-hexane. Specifically, when the Ni content is higher, the number of Ni–Ni ensembles on the Cu–Ni catalyst surface increases, triggering the hydrogen transfer from ethanol to 1-hexene to form *n*-hexane. Thus, although Ni is necessary to increase the catalytic activity, its content should be low so that the Ni atoms in the Cu–Ni alloy are isolated by Cu. The increase in catalytic activity for both the desired hydroboration and undesired hydrogenation by the addition of Ni was attributed to the adsorption strength of alkene, which is very weak on Cu, but enhanced on the Cu–Ni alloy. In turn, the stronger adsorption of alkene increases its concentration on the catalyst surface, thus enhancing the reaction rate. A DFT calculation on the electronic structure of the Cu–Ni alloy (Cu/Ni = 5) clearly described this mechanism. The E_{ad} value of ethylene on pure Cu and on Cu and Ni atoms of Cu–Ni were 0.357 eV, 0.427 eV, and 0.887 eV, respectively (Fig. 11c), indicating that not only the Ni atom itself but also a the Cu atom in the Cu–Ni alloy had a greater ability to adsorb alkene. Thus, a ligand effect of Ni to Cu was observed, which was also reflected in the valence band structure. Ni has intrinsically higher density of state (DOS) at the near Fermi level than Cu (–1–0 eV, Figs. 11d–f) and this trend is more apparent for the atom binding to ethylene (Fig. 11e). However, the Cu atom in the Cu–Ni alloy binding to ethylene has slightly higher DOS in this region compared to pure Cu, probably due to the hybridization of the Ni d-state with Cu (i.e., a ligand effect by the adjacent Ni). As shown in Fig. 11g, the higher d-state reduces the occupation of the anti-bonding state of the metal-adsorbent bond, thus enhancing the adsorption (section 3.3).⁶⁸ Indeed, the bonding and anti-bonding states for the Cu–ethylene bond illustrated in Fig. 11f are lifted up by Ni. Consequently, the electronic and geometric structures can also be controlled by simple alloying.

5.2. Single-atom alloys

One of the advantages of the random alloys is the wide range of the composition ratio that can be used. In an extreme case, a highly biased ratio of 10:1 or 100:1 can also be applied. In this case, as the minor metal is completely isolated by the excess amount of the major metal, it can be considered

as atomically dispersed in the alloy nanoparticle. This alloy type is known as single-atom alloy and has attracted increasing interest as catalyst material.¹³⁶ The metal combination is usually between elements of the groups 10 (Pt,¹³⁷⁻¹³⁹ Pd,¹⁴⁰⁻¹⁴³ Ni:¹⁴⁴ as minor component) and 11 (Au,¹⁴²⁻¹⁴⁴ Ag,¹⁴¹ Cu:¹³⁷⁻¹⁴⁰ as major component), likely because they are all face-centered cubic (FCC) metals and can be easily alloyed, while they are catalytically active (group 10) and inert (group 11) for the target reaction. When the second metal is inert for the target reaction, the isolated active metal shows unique catalytic properties in various reactions. For example, the selective hydrogenation of alkynes^{140, 141, 143} or dienes¹³⁷ can be achieved by isolated Pt or Pd, as the Pt–Pt or Pd–Pd ensembles are completely diluted by the 11-group metal and effectively block the overhydrogenation to undesired products.

We recently reported a different type of a single-atom alloy for highly active catalysis focusing on the NO reduction.¹⁴⁵ Although we have already developed an active and selective catalyst for NO reduction, i.e., the Pd(In_{0.33}Cu_{0.67})/Al₂O₃ pseudo-binary alloy catalyst (section 3.2.1), the reduction in the amount of precious metals, such as Pd and In, would benefit the practical applications. Therefore, we newly designed Cu-rich Cu–Pd/Al₂O₃ (Cu/Pd = 5) catalysts, whose surface consists of Pd isolated by Cu. The isolation of Pd on the surface and bulk was confirmed by FT-IR with CO adsorption and EXAFS analysis, respectively. The peaks assigned to the stretching vibration of CO adsorbed on the Pd bridge and hollow sites decreased with increasing Cu content and disappeared at a Cu/Pd ratio of 5.¹⁴⁵ Besides, only the Pd–Cu scattering without Pd–Pd scattering was observed in the Fourier transform of the Cu–Pd/Al₂O₃ (Cu/Pd = 5, Fig. 12b) EXAFS spectrum. The catalytic performance of Pd was drastically improved after alloying with an excess Cu amount. In particular, Cu–Pd/Al₂O₃ (Cu/Pd = 5) exhibited 100% NO-to-N₂ conversion in the NO–CO reaction even at 200 °C, whereas Pd/Al₂O₃ afforded only 3% conversion to N₂ (Fig. 12c). The catalytic performance of Cu–Pd/Al₂O₃ was also tested in the presence of O₂ and a hydrocarbon (C₃H₆) as a more practical condition for NO_x removal (deNO_x) from automobiles (three-way catalyst (TWC) condition). The Cu–Pd/Al₂O₃ catalyst exhibited a much higher catalytic performance than Pd/Al₂O₃ with a minimum formation of N₂O even under the TWC condition (Fig. 12d). It should be noted that Cu–Pd/Al₂O₃ showed a catalytic performance comparable to that of Pd/Al₂O₃, although Pd/Al₂O₃ included ten times the equimolar Pd amount of Cu–Pd/Al₂O₃ (labeled as Pd×10). Thus, the developed single-atom

alloy catalyst enabled an efficient and selective deNO_x, but also a significant decrease in the noble metal use to one-tenth. A mechanistic study based on kinetic analysis and DFT calculation revealed an interesting difference in the reaction mechanism between Pd-rich and Cu-rich catalysts. Specifically, over Pd-rich catalysts, an NO molecule is dissociated to N and O atoms, followed by the association of two N-atoms to form N₂ (the standard mechanism for Pd-based catalysts), while two NO molecules are coupled over Cu-rich catalysts to form an (NO)₂ dimer, followed by N–O scissions ((NO)₂ → N₂O + O and N₂O → N₂ + O) with low energy barriers. Fig. 12e shows the energy diagrams of NO reduction at the step sites of Cu(211) and Pd-doped Cu(211) surfaces. The energy barrier of the rate-determining step, i.e., the N–O scission of the (NO)₂ dimer, decreased by Pd-doping (DFT: 0.66→0.46 eV and 63.7→44.4 kJ mol⁻¹, experimental: 61→43 kJ mol⁻¹). Thus, isolated Pd does not act as an active site, but a strong promoter for Cu. It should also be noted that the promoted Cu is more active than pure Pd. Besides, the amount of Pd should be sufficiently low, otherwise a large number of Pd species will form Pd–Pd ensembles, which no longer act as promoters for Cu, but as reaction sites with lower performance.

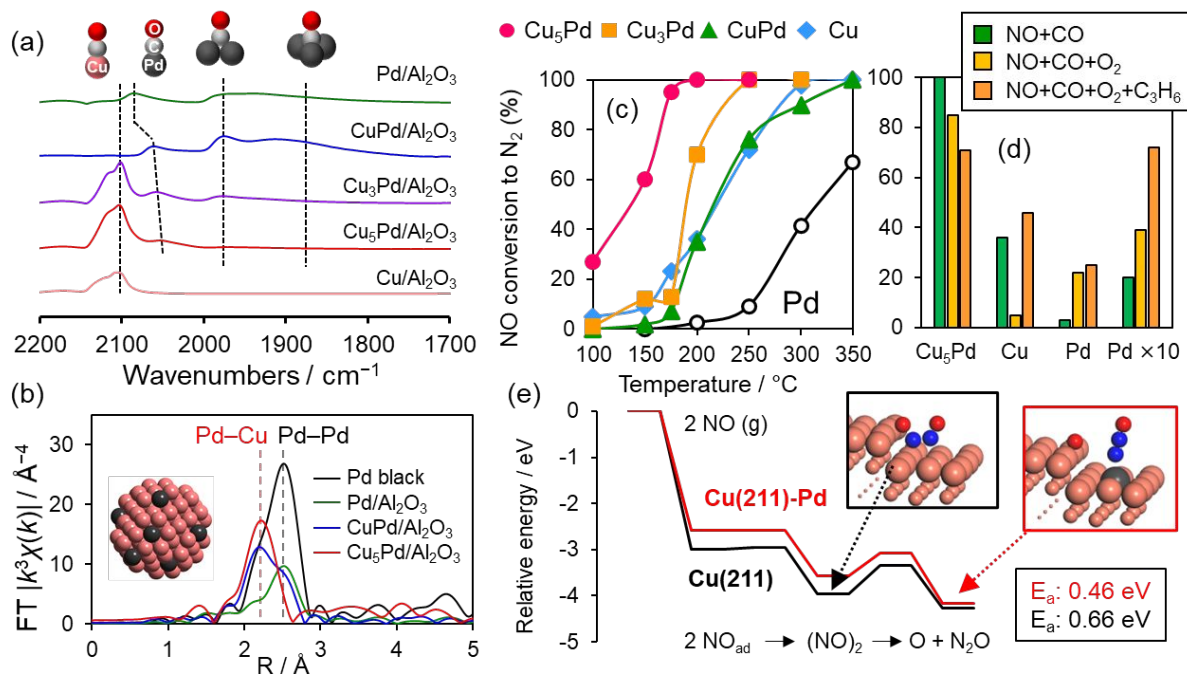


Fig. 12. (a) FT-IR spectra of CO adsorbed on the Cu–Pd/Al₂O₃ catalysts. (b) Fourier transforms of the Pd K-edge EXAFS spectra of the Pd and Cu–Pd catalysts. (c) NO-to-N₂ conversion (%) during NO reduction by CO over Pd, Cu, and Cu–Pd catalysts as a function of the reaction temperature (NO, CO: 0.5%, GHSV = 80,000 h⁻¹). (d) NO-to-N₂ conversion (%) during NO reduction by CO in the

presence of O₂ and C₃H₆. (e) Energy diagrams of NO reduction over Cu(211) and Pd-doped Cu(211) surfaces calculated by DFT.

5.3. High-entropy alloys

High-entropy alloys (HEAs) are widely defined as solid–solution alloys containing at least five different elements, each with an atomic fraction between 5–35%.¹⁴⁶ More specifically, those alloys of which mixing entropy (eq. 1) exceeds 1.5 R are called HEAs:¹⁴⁶

$$\Delta S_{mix} = -R \sum_{i=1}^n X_i \ln X_i \quad (1)$$

where, ΔS_{mix} is the mixing entropy, R is the gas constant, X_i is the molar ratio of component i , and n is the total number of elements involved. Considering a solid–solution alloy with random mixing in an equal ratio, ΔS_{mix} increases in a logarithmic fashion with increasing n ($\Delta S_{mix}/R = 0, 0.69, 1.10, 1.39, 1.61, \text{ and } 1.79$ for $n = 1, 2, 3, 4, 5, \text{ and } 6$, respectively). This entropy effect allows the mixing of two or more immiscible metal elements (section 5.1), resulting in a multimetallic solid–solution alloy, which significantly expands the design options of alloy-based catalysts. However, due to the difficult synthesis of nanoparticulate HEAs with high uniformity, very few papers have so far reported their properties in catalysis.

Very recently, Yao *et al.* reported a carbothermal shock (CTS) synthesis method as an innovative protocol for the preparation of nanoparticulate HEAs.¹⁴⁷ A carbon nanofiber support, that was impregnated with several metal precursors (chlorides), was subjected to an electrical pulse (55 ms) under Ar atmosphere to induce ultrafast Joule heating ($\sim 10^5 \text{ K s}^{-1}$) to about 2000 K. The precursor salts are easily decomposed to liquid metal mixtures due to high temperature, followed by rapid quenching to form well mixed multimetallic solid–solution alloys. Thus, the synthesis of quinary (PtFeCoNiCu and PtPdCoNiFe) up to octonary (PtPdCoNiFeCuAuSn) HEAs with narrow size distributions (10 or 20 nm) is allowed. It should also be noted that the octonary HEAs consist of various elements with diverse atomic radii (1.24 to 1.44 Å), reduction potentials (−0.25–1.5 V vs. SHE), preferred crystal structures (FCC, body-centered cubic, hexagonal close-packed, or tetragonal), and melting points (500–2000 K). In this study, a quinary HEA consisting of PtPdRhRuCe nanoparticles was prepared and tested for NH₃ oxidation. The HEA catalyst showed 100% NH₃ conversion and >99% NO_x (NO + NO₂) selectivity at 700 °C, whereas the corresponding

penta-metallic catalyst prepared by the conventional wet impregnation method gave a poor NO_x yield of 17.8%.

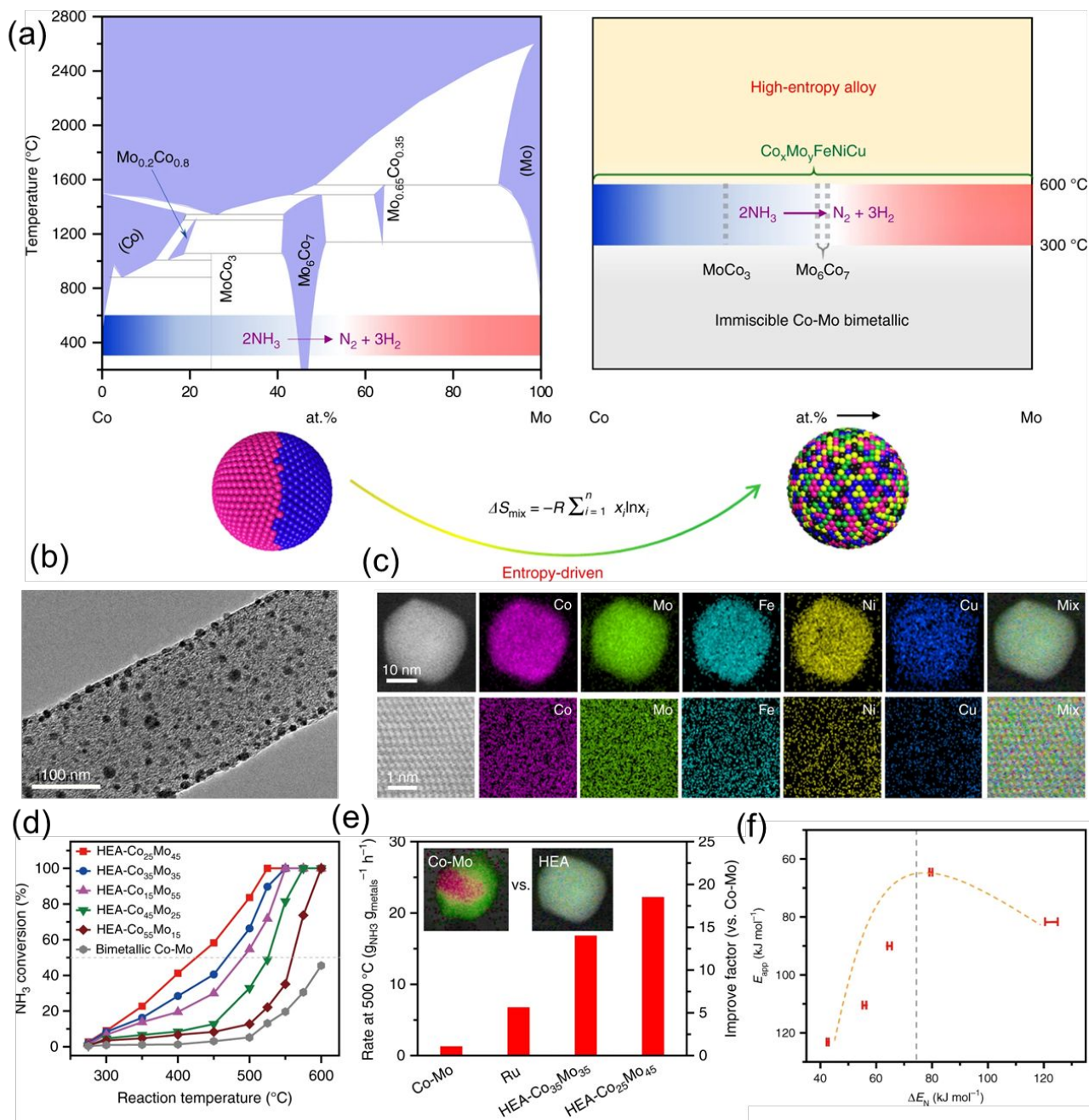


Fig. 13. (a) HEA catalysts addressing the miscibility limitation of conventional binary alloys. (b) TEM images of the obtained HEA nanoparticles dispersed on carbon nanofibers (CNFs). (c) High-resolution STEM-based elemental maps of the HEA- $\text{Co}_{25}\text{Mo}_{45}$ nanoparticles. (d) Change in the NH_3 (5 vol%) conversion rate over different HEA- Co_xMo_y nanoparticles and bimetallic Co-Mo (Co/Mo = 25/45) depending on the reaction temperature (space velocity = $36 \text{ L gcat}^{-1} \text{ h}^{-1}$). (e) Comparison of reaction rates measured in the kinetic regime among bimetallic Co-Mo, Ru, and HEA- Co_xMo_y catalysts ($T = 500 \text{ }^\circ\text{C}$). The inset shows elemental maps for the bimetallic Co-Mo (Co/Mo = 25/45) and HEA- $\text{Co}_{25}\text{Mo}_{45}$ catalysts. (f) Correlation between ΔE_N (recombative desorption energy of nitrogen) and apparent activation energy (E_{app}) showing a volcano-type behavior for the HEA- Co_xMo_y catalysts, where HEA- $\text{Co}_{25}\text{Mo}_{45}$ was close to the peak position. Reproduced with permission.¹⁴⁸ Copyright 2019 Springer Nature.

In a subsequent study,¹⁴⁸ Yao *et al.* clearly demonstrated the effective use of HEAs-based catalysts to address the miscibility limitation. They mainly focused on the Co–Mo bimetallic system, which has been known as a promising catalyst platform for NH₃ decomposition to H₂ and N₂. However, as shown in Fig. 13a, only two intermetallic Co₃Mo and Co₇Mo₆ phases were observed in the Co–Mo bimetallic system at temperatures lower than 800 °C, which motivated further catalytic studies on optimizing the Co–Mo ratio. Thus, a series of quinary HEAs with the general composition of Co_xMo_yFe₁₀Ni₁₀Cu₁₀ (Co_xMo_y-HEA; $x/y = 15/55, 25/45, 35/35, 42/25, \text{ and } 55/15$, Figs 13b–d), were prepared and tested in the decomposition of diluted NH₃ (5% NH₃/He).¹⁴⁸ As depicted in Fig. 13e, the optimized catalyst Co₂₅Mo₄₅-HEA showed three and 19 times higher reaction rates than Ru and bimetallic Co–Mo (phase-separated) catalysts, respectively. Further kinetic studies suggested that the adsorption energy of the N-atom determined the catalytic activity (Fig. 13f), as a weak adsorption (Co-rich) increases the energy barrier for N–H bond cleavage, whereas a strong adsorption inhibits the N₂ desorption. Thus, it was revealed that the HEA-based designed catalyst allows the effective tuning of the surface adsorption properties by constantly changing the alloy composition.

Prompted by the successful results in the catalytic use of HEAs, the number of studies and relevant publications are expected to increase in the near future. However, some obstacles in material synthesis should be addressed for a wider application of nanoparticulate HEAs in catalysis. For example, developing a new synthetic approach as an alternative to the CTS method, which is also applied to insulating materials, is highly desirable, so that conventional metal oxides, such as SiO₂, Al₂O₃, MgO, etc., can be used as catalyst supports for a variety of conditions and target reactions. A further breakthrough in material synthesis will boost the rise of this research field.

6. New materials generated by chemical treatment to alloys

Intermetallic compounds used in catalysis generally consist of catalytically active (late transition) and chemically labile (early transition or typical) metals. Therefore, in some cases, the parent intermetallic phase is chemically transformed to a different structure through redox reactions. These transformations are completely different from phase transition and occur either during catalytic

reactions in the presence of corrosive chemicals or due to a chemical treatment based on a synthetic protocol. In the first case, the oxidative decomposition of intermetallic compounds into a composite of the active metal and an oxide of the second metal ($A_xB_y \rightarrow xA + yBO_2$) often occurs when oxygen or moisture is involved in the catalytic reaction.^{47, 149, 150} The second case is described in this section, where we present novel synthetic protocols that apply chemical treatments to intermetallic compounds, generating unique and complex nanostructures for effective catalysis. Two types of chemical treatments can be performed, where the structural modification occurs either on the outermost surface or in the wider region including the sub-surface or the bulk of the intermetallic compound.

6.1. Surface decoration to intermetallic compounds

The surface structures and chemical properties of intermetallic compounds can be modified by "decorating" the metal atoms of the outermost surface, e.g., by replacing a constituent metal with a different metal or depositing a third element on a specific site. In a broader sense, Pt-skin structures formed by electrochemical dealloying of Pt–3d metal alloys¹⁵¹⁻¹⁵³ could also be classified into this category. Our research team has also recently developed a synthetic method based on galvanic replacement for the surface decoration of intermetallic compounds.¹⁵⁴ When the oxidation potential of the second metal (M) is lower than that of the third metal (N), the M atoms on the outermost surface are replaced by N-atoms through the redox reaction described in Eq. (2):



Therefore, we applied this phenomenon to the PdZn system with Pb as the modifier for Zn and observed that Pb-modified PdZn (PdZn–Pb) acted as a highly selective catalyst for alkyne semihydrogenation (Fig. 14a).¹⁵⁴ For the galvanic replacement, an aqueous solution of $Pb(NO_3)_2$ was added to PdZn/SiO₂, which was pre-reduced by H₂ at 400 °C in a round-bottom flask and then cooled to room temperature, followed by washing with water and drying. The amount of Pb²⁺ in the solution was adjusted so that the Pb/Pd ratio is 0.25. The combination of HAADF–STEM–DEX analysis and XPS studies with Ar⁺ sputtering revealed that the bulk part of the nanoparticles retained the parent PdZn structure, while Pb was localized on the surface of nanoparticles (Figs. 14b-d). The FT-IR study with CO adsorption indicated that no Pd segregation occurred to form Pd–Pd ensembles

on PdZn–Pb/SiO₂. We also performed an EXAFS study for Pb L_{III}-edge, where the curve-fitting analysis indicated a coordination number of 4.2 for Pb–Pd scattering. This suggests that Pb replaced the Zn atoms in the ZnPd₄ sites at the most stable PdZn(101) surface. Fig. 14e shows the results of phenylacetylene hydrogenation using PdZn–Pb/SiO₂ and Pd–Pb/CaCO₃ (Lindlar catalyst). For the Lindlar catalyst, the styrene selectivity sharply dropped after the complete conversion of phenylacetylene, while a high styrene selectivity was retained when PdZn–Pb/SiO₂ was used. This result clearly shows that PdZn–Pb/SiO₂ can more effectively prevent the overhydrogenation of styrene to ethylbenzene compared to the conventional Lindlar catalyst. Thus, we modeled the Pb-substituted PdZn(101) surface, where the Pb–Pd coordination number is four, and calculated the adsorption states of alkyne and alkene.

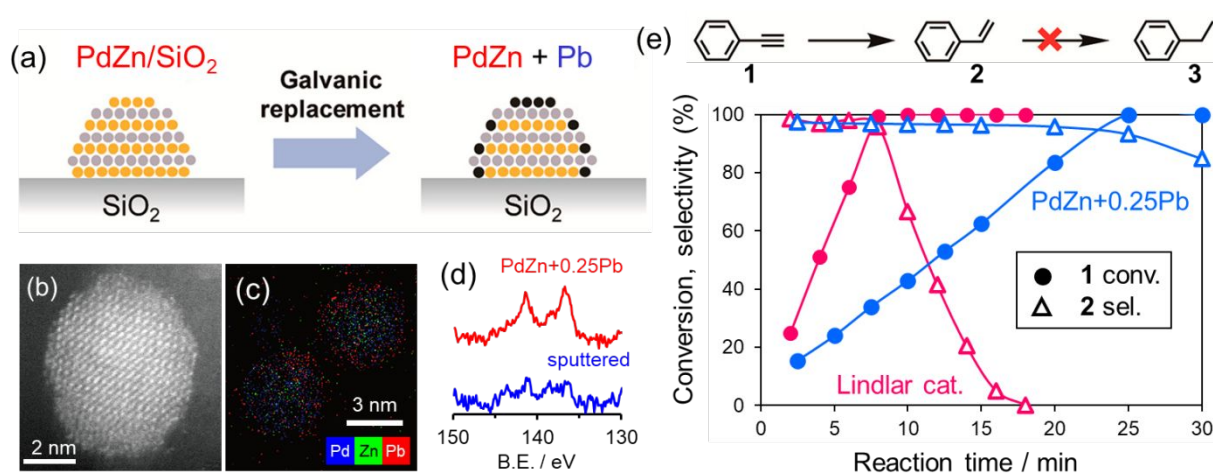


Fig. 14. (a) Illustration of the surface modification of intermetallic PdZn nanoparticles using the galvanic replacement of Zn by Pb for its catalytic application on the selective semihydrogenation of phenylacetylene. (b) HAADF–STEM image of a single PdZn+0.25Pb/SiO₂ nanoparticle and (c) elemental maps of the Pd/Zn/Pb overlayer obtained by EDX. (d) Pb 4f XPS spectra of PdZn+0.25Pb/SiO₂ before and after Ar sputtering. (e) Time-conversion and selectivity curves over the PdZn+0.25Pb and Lindlar catalysts recorded for the hydrogenation of phenylacetylene.

Unlike ethylene, acetylene could be adsorbed on the Pb-modified Pd site, indicating that the desorption of ethylene is significantly promoted and its re-adsorption is also prevented., which is consistent with the catalyst's high ability to inhibit the alkene overhydrogenation. This can be attributed to the high steric hindrance of the Pd site by the large Pb atoms (Pb–Pd length: 2.77 Å) that do not allow the adsorption of alkene. Although a similar reaction environment using Pd–Pb materials such as intermetallic Pd₃Pb, Pd₅Pb₃, PdPb, or the Lindlar catalyst would be expected to be

efficient, Pd–Pb intermetallics have longer Pd–Pb bonds than PdZn–Pb (2.85–2.95 Å), probably due to the lattice expansion by the Pb atoms in the bulk, indicating the lower steric hindrance of Pd. Therefore, the surface decoration approach allows the generation of a highly constrained reaction environment that cannot be arranged by pure intermetallic compounds.

Very recently, we have developed a different type of surface-decorated intermetallic compounds using PtGa and Pb for propane dehydrogenation (PDH).¹⁵⁵ The stable (111) plane of intermetallic PtGa has four different surface terminations with three-fold and isolated Pt and Ga, which are indicated as Pt₃, Ga₃, Pt₁, and Ga₁, respectively (Figs. 15a and 15b). Although both Pt sites are active for C–H activation of light alkanes, the Pt₃ sites also trigger undesired side reactions that form coke and deactivate the catalyst.

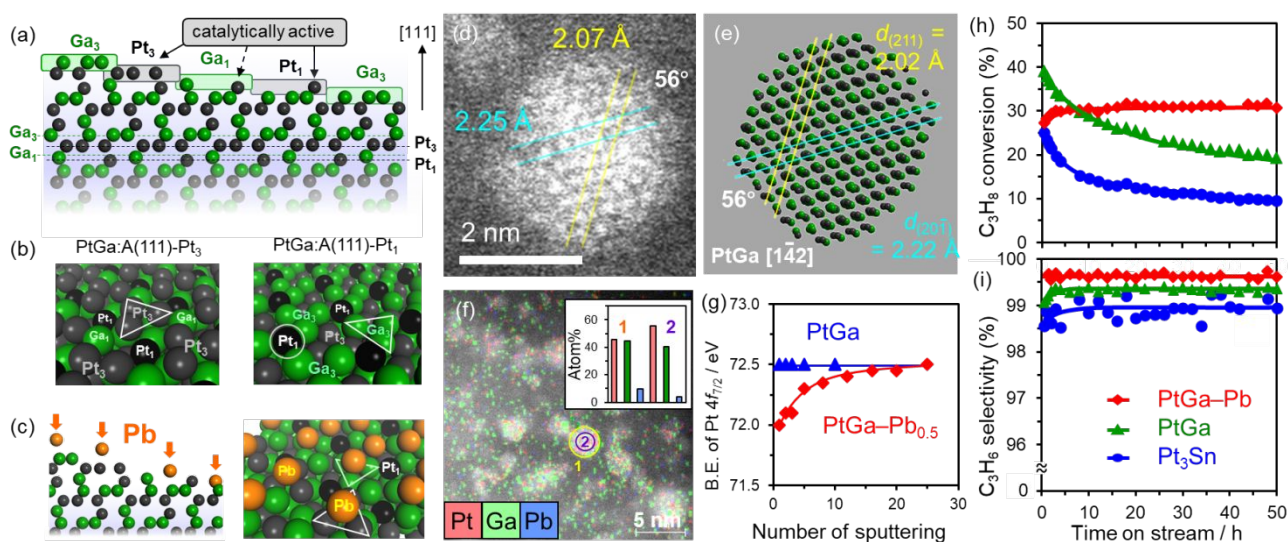


Fig. 15. (a) Four different surface terminations of PtGa:A(111) viewed along the [101] direction (ball model). (b) Diagonal view of Pt₃ and Pt₁ termination (space-filling model). Pt₁ is indicated with black color. (c) Catalyst design by Pb deposition to block the Pt₃ (Ga₃) sites and keep the Pt₁ sites available. (d) HAADF-STEM image of a single nanoparticle in PtGa–Pb/SiO₂ (Pt/Pb = 2). (e) Crystal structure of intermetallic PtGa viewed along the [142] direction. (f) Elemental map of Pt, Ga, and Pb recorded by EDX. The inset shows their atom% included in areas 1 (yellow circle) and 2 (purple circle), corresponding to the whole and core region of a single nanoparticle. (g) Changes in Pt 4f_{7/2} binding energy (B.E.) of PtGa/SiO₂ and PtGa–Pb/SiO₂ (Pt/Pb = 2) during sputtering cycles. Changes in (h) propane conversion and (i) propylene selectivity in PDH catalyzed by PtGa/SiO₂, PtGa–Pb/SiO₂ (Pt/Pb = 2), and Pt₃Sn/SiO₂. The catalyst amounts were adjusted so that the number of exposed Pt is identical (4.5 μmol): PtGa (9.0 mg), PtGa–Pb (Pt/Pb = 2) (15 mg), Pt₃Sn (3.7 mg). Gas feed: C₃H₈/H₂/He = 3.9:5.0:40 mL min⁻¹. Temperature: 600 °C.

In contrast, Pt₁ sites are much less active for the side reaction than Pt₃ sites. Therefore, a highly selective and stable catalyst for alkane dehydrogenation can be synthesized, provided that only the Pt₃ sites are disabled by the deposition of the third metal (Fig. 15c), while the Pt₁ sites remain intact. In our study, we found that Pb acted as an effective modifier for this purpose and the resulting PtGa–Pb catalyst was a very stable and selective catalyst for PDH at high temperature. In this system, the appropriate amount of Pb was co-impregnated with Pt and Ga (Pt/Ga/Pb = 1/1/0.5) on SiO₂, followed by calcination in air at 400 °C and the subsequent H₂ reduction at 700 °C (not by successive impregnation of Pb to PtGa), generating intermetallic PtGa nanoparticles (2–3 nm, Figs. 15d and 15e) with Pb decorated surfaces. It should be noted that this structure was formed spontaneously during the preparation at high temperature, indicating that the Pb atoms are preferably present on the surface and not in the bulk, probably due to the larger atomic radius of Pb (Pt: 1.385 Å, Ga: 1.408 Å, and Pb: 1.746 Å).⁷⁵ The absence of Pb in the bulk of the PtGa nanoparticles was confirmed by EDX mapping and XPS analysis with Ar⁺ sputtering (Figs. 15f and 15g). We also performed FT-IR analysis with CO adsorption, which revealed that the Pt₃ sites were selectively blocked by the Pb deposition, whereas the Pt₁ sites remained open for CO adsorption. Figs. 15h and 15i show the catalytic performance of PtGa/SiO₂, PtGa–Pb/SiO₂, and Pt₃Sn/SiO₂ in PDH at 600 °C. Pt₃Sn, a well-known Pt–Sn catalyst for light alkane dehydrogenation, was rapidly deactivated within the first 10 h, suggesting that the reaction conditions were very harsh. PtGa exhibited a similar deactivation trend, indicating that the undesired coke generation reactions occur over the Pt₃ sites. However, the PtGa–Pb catalyst maintained the high propane conversion (30%) and propylene selectivity (99.6%) for at least 50 h without deactivation.¹⁵⁵ The reaction was conducted for up to 96 h with almost no deactivation. Furthermore, a temperature-programmed oxidation experiment for the spent catalyst (50 h) revealed that the amount of coke accumulated on the catalyst decreased to approximately 1/8 by the Pb deposition to PtGa, demonstrating the successful inhibition of coke formation. We also performed DFT calculations for the C–H activation steps (C₃H₈ → C₃H₇ + H → C₃H₆ + 2H → C₃H₅ + 3H) and the propylene desorption over the Pt-based materials. It is known that the propylene selectivity generally depends on the difference in the energy barrier (ΔE) between the propylene desorption and the third C–H activation step (C₃H₆ → C₃H₅ + H). Thus, propylene is either desorbed as a product or is decomposed by subsequent bond scissions. The

Pt₁ site in PtGa gave a ΔE value of 64.9 kJ mol⁻¹, which was much higher than that of the Pt₃ sites in PtGa and Pt₃Sn (35.9 and 24.1 kJ mol⁻¹, respectively), demonstrating the outstandingly high selectivity of the Pt₁ sites for propylene production.

Thus, the surface modification concept enables the development of significantly active and selective catalytic systems that cannot be prepared using pure alloy materials. To design and construct such a favorable reaction environment, one needs to understand the stability and atomic arrangement of the surface structure, as well as the appropriate method for the surface modifications.

6.2. Unique nanostructures formed by decomposition of intermetallic compounds

When an intermetallic compound including a labile metal is subjected to a harsh chemical treatment, the catalyst structure is often drastically changed to form a unique nanostructure. Raney Ni is a well-known example of this chemical transformation.¹⁵⁶ Bulk Ni–Al powder can be treated with a strong basic solution to leach Al, resulting in the formation of a porous Ni material,¹⁵⁶ which can be subsequently used as an active catalyst for various reactions such as hydrogenation^{157, 158} and reforming.¹⁵⁹ Similar dealloying techniques using a strong base can be applied for the treatment of other 3d-transition metals (e.g., Fe)¹⁶⁰ and/or trimetallic systems. Kameoka et al. reported that dealloying of Al₇₆Fe_{23.5}Pt_{0.5}¹⁶¹ by an aqueous NaOH solution afforded a Pt–Fe₃O₄ nanocomposite consisting of highly dispersed Pt and a porous Fe₃O₄ matrix, which was more active than the conventional Pt/Fe₃O₄ catalyst for CO oxidation and preferential oxidation of CO in excess H₂.¹⁶² Abe and coworkers also reported that nanoporous Ni/Y₂O₃ could be obtained by dealloying Ni_{12.5}Y_{12.5}Al₇₅, which exhibited higher catalyst stability than the conventional Ni/Al₂O₃ catalytic system.¹⁶³ In addition, we disclosed a similar catalytic system based on dealloying, where the ternary intermetallic compound Ru₂LaAl₁₀ was used for the synthesis of Ru–La₂O₃.¹⁶⁴ This porous composite exhibited higher catalytic activity than Raney Ru prepared from Ru₄Al₁₃. Therefore, in this section, we present unique nanostructures obtained from intermetallic compounds that are entirely different from the conventional Raney-type porous materials.

6.2.1. Ni clusters embedded in SiO₂ matrix

This material was serendipitously found. In this study, we originally intended to prepare a Ni-skin structure on a Ni–Si intermetallic compound by dealloying using a dilute aqueous solution of hydrofluoric acid (HF). The synthetic procedure is very simple; a bulk NiSi_2 powder with a mean particle size of 50 μm was added in a vigorously stirred 1.0 M HF solution and kept for 15 min at room temperature in the air, followed by washing with water, drying, and H_2 reduction at 400 $^\circ\text{C}$ for 0.5 h.¹⁶⁵ After the process completion, the bulk NiSi_2 structure was retained, because the acid treatment was fast and was performed at low concentration and temperature. However, the resulting near surface structure was not the expected. Figs. 16a–e show the results of HAADF–STEM–EDX analysis that focused on the near surface region of the HF-treated NiSi_2 ($\text{NiSi}_2\text{-HF}$), and a schematic illustration of the structural change during the HF treatment.

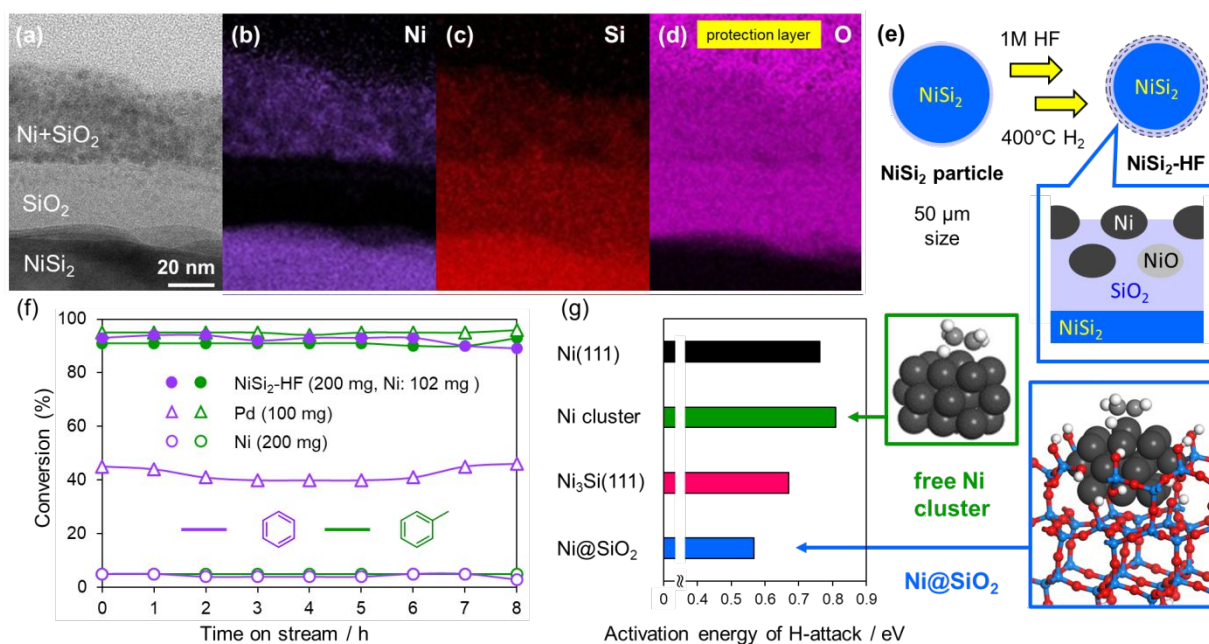


Fig. 16. (a) HAADF–STEM image of the near surface region of $\text{NiSi}_2\text{-HF}$ and elemental maps of (b) Ni, (c) O, and (d) Si. The organic protection layer used for the sample preparation by focused ion beam is observed as C and O. (e) Schematic illustration of the near surface structure change upon HF treatment and the subsequent H_2 reduction. (f) Change in the reactant conversion during the hydrogenation of benzene and toluene over $\text{NiSi}_2\text{-HF}$, Pd black, and Ni catalysts at 150 $^\circ\text{C}$. The selectivity for cyclohexane or methylcyclohexane was 100% for each catalyst. (g) Activation energies of the hydrogen attack on ethylene adsorbed on Ni(111), $\text{Ni}_3\text{Si}(111)$, a Ni_{20} cluster, and a Ni_{20} cluster embedded in a SiO_2 matrix (Ni@SiO_2), as calculated by DFT. Transition-state structures are also shown.

Several small Ni clusters (2–5 nm) embedded in the SiO_2 matrix (Ni@SiO_2) at the near surface region were observed, while the SiO_2 layer of 50–60 nm thickness (in depth) was also formed on the

bulk NiSi₂. The resulting NiSi₂-HF catalyst exhibited 14–24 and 7–8 times higher reaction rates and TOF values, respectively, than the pure Ni powder in the hydrogenation of various unsaturated hydrocarbons (ethylene, acetylene, toluene, and benzene). It should also be highlighted that NiSi₂-HF showed a long-term stability and higher TOF than the pure Pd powder in benzene hydrogenation (Fig. 16f). Thus, it was proven that the catalytic activity of non-noble Ni can be significantly enhanced and surpass Pd by appropriately using earth-abundant Si, demonstrating the validity of this approach for the preparation of noble-metal-alternative catalysts. Given that cycloalkanes obtained as main products from aromatic hydrogenation, such as cyclohexane and methylcyclohexane, are considered as promising hydrogen carriers, NiSi₂-HF can be used for hydrogen storage applications as a promising noble-metal-alternative material. DFT calculations suggested that the SiO₂ matrix surrounding the Ni cluster has a specific promotion effect on hydrogenation. As shown in Fig. 16g, the activation energy (E_a) of the hydrogen attack on ethylene adsorbed on Ni@SiO₂ was much lower than that required for the attack on ethylene on the Ni(111) terrace and the free Ni cluster. Comparing the transition states of the hydrogen attack on Ni@SiO₂ and the free Ni cluster, the Ni atom adsorbing ethylene in Ni@SiO₂ was higher and closer to ethylene than that in the free Ni cluster, which stabilized the transition state of the hydrogen attack and significantly lowered E_a . Moreover, a possible electronic effect contributing to this stabilization was excluded based on the XPS study that showed no difference in the electronic states of the surface Ni atoms between NiSi₂-HF and pure Ni. This stabilization could be explained by a strain effect caused by the surrounding SiO₂ matrix.

6.2.2. Rooted catalysts

Abe *et al.* have recently reported unique phase-separated nanocomposites of Ni and Y₂O₃ (Ni#Y₂O₃) prepared from intermetallic NiY, which were considerably different from the conventional heterogeneous supported metal catalysts.¹⁶⁶ The Ni#Y₂O₃ nanocomposites consisted of an entangled network of fibrous metallic Ni and Y₂O₃, which was developed out of the bulk part, leading to a rooted structure (Figs. 17a–d).¹⁶⁶ The rooted structure was obtained by heating NiY in the presence of CO and O₂. A possible mechanism for the nanophase separation was initiated by the dissociation of molecular oxygen. The resulting O-atom was then spilled over the surface and diffused into the

bulk to form the Y_2O_3 phase, whereas Ni retained its metallic state via the reduction by CO. The morphology and topology of the nanocomposites could be controlled by tuning the treatment temperature and the CO/O₂ ratio. The rooted Ni# Y_2O_3 catalyst exhibited a significantly high stability when applied to the low-temperature CO₂ reforming of methane for at least 1000 h (Fig. 17e).

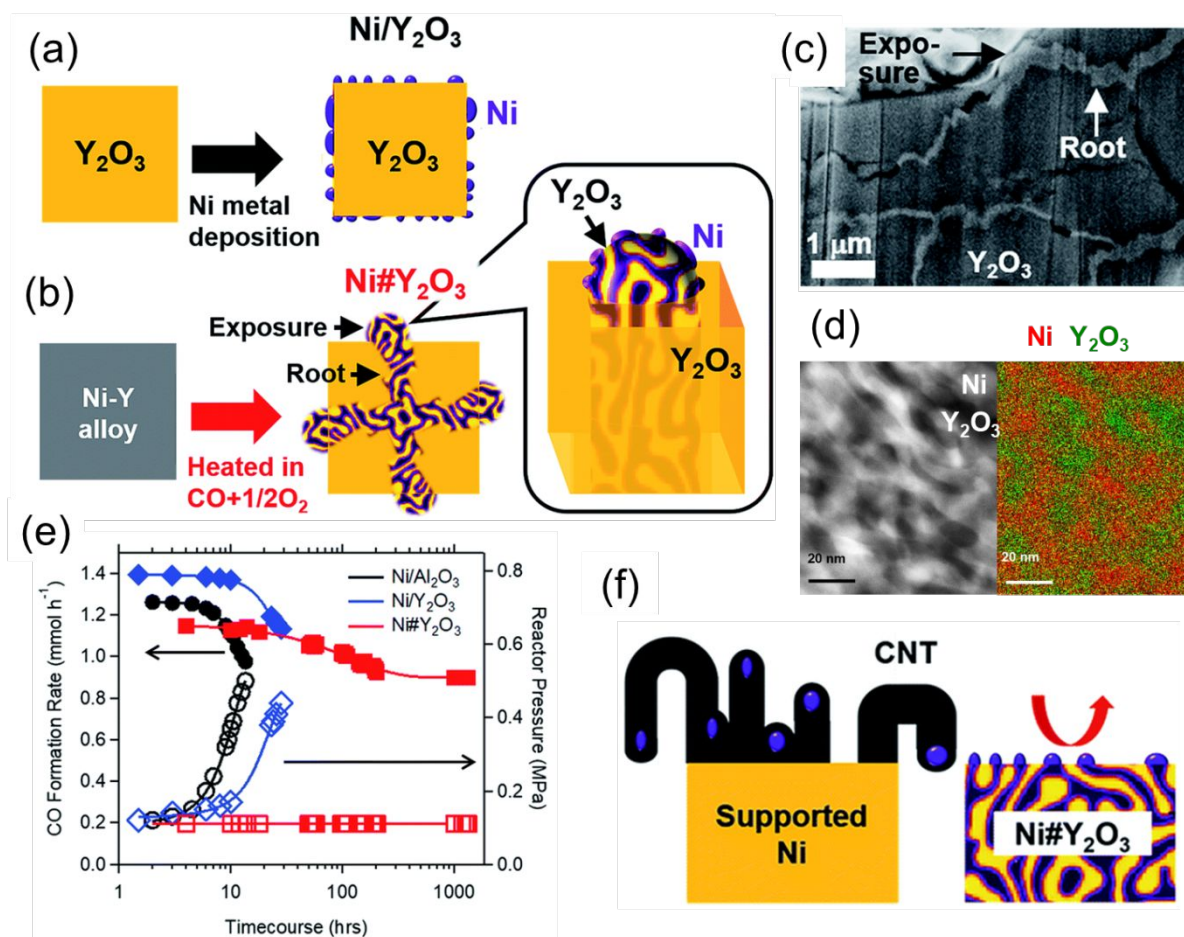


Fig. 17. (a) Traditional supported catalysts, such as Ni/ Y_2O_3 , are prepared by depositing Ni nanoparticles on the surface of the support. (b) The rooted Ni# Y_2O_3 catalyst was prepared by melting Ni and Y metals into a Ni–Y alloy under Ar, followed by heating of the prepared Ni–Y alloy under a CO/O₂ atmosphere. (c) Cross-section SEM image of a single Ni# Y_2O_3 particle, showing the distribution of the rooted structure in the bulk. The black arrow indicates one of the exposures of the rooted structure. (d) (left) High-magnification HAADF–STEM and (right) elemental mapping images of the rooted structure. (e) Catalytic performance of Ni# Y_2O_3 and supported Ni catalysts and change in the reactor pressure during dry reforming of methane: catalyst amount = 0.1 g; reaction temperature = 723 K; CH₄/CO₂/Ar = 1/1/98 in vol%; flow rate = 100 mL min⁻¹. (f) A model for the inhibited CNT growth over the Ni# Y_2O_3 catalyst due to the topological immobilization of the Ni catalysis center. Reproduced with permission.¹⁶⁶ Copyright 2019, Royal Society of Chemistry.

Instead, the conventional Ni/ Y_2O_3 and Ni/Al₂O₃ catalysts were rapidly deactivated in 10 h due to the inhibition of mass transport by coke accumulation. Thus, an *in situ* TEM analysis was performed to

investigate the carbon formation on Ni/Al₂O₃ during the catalytic run, which showed a rapid growth of multi-walled carbon nanotubes generated from freely migrating Ni nanoparticles over the Al₂O₃ support. This carbon growth was not favored on Ni#Y₂O₃, because the active Ni site was anchored in the highly entangled nanocomposite network through the rooted structure, as depicted in Fig. 29f. The hard X-ray photoelectron spectroscopy analysis revealed that the Y₂O₃ moiety in Ni#Y₂O₃ had a higher amount of oxygen vacancies than Ni/Y₂O₃, while it was also suggested that the oxygen-deficient Y₂O₃ contributed to the elimination of carbon deposits in the Ni–Y₂O₃ interface.

A similar bimetallic system of Ni₃Nb has also been reported¹⁶⁷ for the preparation of phase-separated Ni#NbO_x nanocomposites. The rooted structure was formed during the catalytic use of intermetallic Ni₃Nb in the NO–CO reaction. In this case, NO seems to act as an oxygen source (2NO → N₂ + 2O), like O₂ in the NiY system, leading to the oxidization of Nb, while CO preserves the metallic state of Ni. The Ni#NbO_x catalyst showed a remarkably higher catalytic activity for the NO–CO reaction than pure Ni, Nb, and Pt. Moreover, a long-term stability test at 400 °C revealed that Ni#NbO_x selectively converted NO to N₂ for 500 h without losing its catalytic performance. The high catalyst stability was attributed to the rooted Ni structures in the NbO_x matrix. It was also suggested that the oxygen vacancies in NbO_x served as carriers of N-atoms, promoting N migration and N₂ recombination.

In summary, the rooted catalysts provide high catalyst durability for long-term use under harsh conditions. Although their structures look very complex, they might be controlled by a topological analysis, which can be developed based on experimental parameters such as temperature, concentration, and the characteristics of the chemicals.

7. Concluding remarks

In this paper, we presented a series of our recent developments in the chemistry of alloy materials for catalytic use. The described alloys were classified into various categories, such as ordered and random, based on their structural differences. Other important and emerging alloy materials developed by other researchers, which could be used as next-generation materials for catalysis, were also mentioned and categorized. It has been observed that the structural geometry of ordered alloys changes drastically with high regularity, preventing undesired reaction paths and/or promoting the

desired reaction process. Specific atomic alignments of some intermetallic compounds can also efficiently control the adsorption conformation of the reactant molecules and their surface dynamics, allowing highly challenging molecular transformations such as stereo-, chemo-, and regioselective hydrogenation. Thus, the regularity and the specific geometry of the developed ordered materials plays an important role in enhanced catalysis. Instead, electronic factors significantly affect the catalytic processes on both ordered and random alloys. Random alloys do not have specific geometric effects, but allow great flexibility in choosing the appropriate composition ratio. A highly biased composition ratio allows the isolation of the main active metal by an excess amount of the counterpart metal, leading to single-atom alloys with unique properties for challenging chemical transformations. In addition, the entropic effect increases the possible number and combination of the constituent metals that can be used. Pseudo-binary or Heusler alloys have the advantages of both ordered and random alloys, i.e., specific surface structures and tunability of the composition ratio and catalytic performance. The combination of three metal elements adjacent at the atomic level with high regularity provides multifunctional active sites for the development of highly active, selective, and durable catalytic systems. Furthermore, alloys can be used as starting materials for the preparation of complex metal–metal-oxide nanocomposites through various chemical treatments, which exhibit remarkably high catalytic activity or stability. It is thus clear that a variety of alloy materials have already been developed for the preparation of efficient catalytic systems. However, the design of catalysts based specifically on the principles of metallurgy, surface science, catalytic chemistry, and materials chemistry is essential for the realization of the desired catalytic systems. In particular, the design of catalytic systems for specific reactions requires (1) a deep understanding of each element's nature, (2) the prediction of the resulting crystal (or composite) structure and surface atomic arrangement, and (3) the successful identification of the element or factor that should be optimized. The synthetic procedures should also be improved to obtain the complex alloy nanoarchitectures as fine and uniformly dispersed nanoparticles. Moreover, as the application of alloy materials in catalytic chemistry is currently evolving, innovative studies in their synthetic methodology will further boost this research field.

Acknowledgements

This work was supported by JSPS KAKENHI (Grant Numbers 26820350, 17H01341, and 17H04965) and by MEXT within the projects “Integrated Research Consortium on Chemical Sciences (IRCCS)” and “Elements Strategy Initiative (JPMXP0112101003)”, as well as by the JST CREST (JPMJCR17J3) and PRESTO projects (JPMJPR19T7).

Conflicts of interest

There are no conflicts to declare.

References

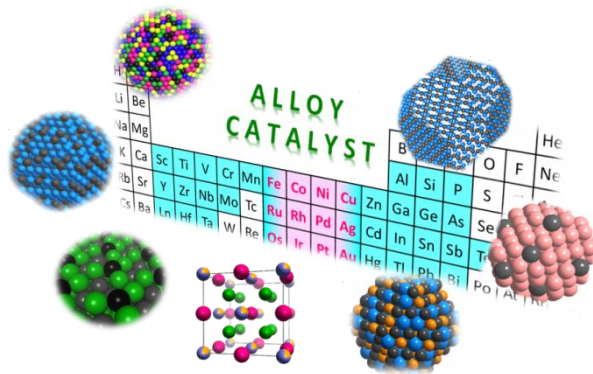
1. G. V. Smith and F. Notheisz, *Heterogeneous catalysis in organic chemistry*, Academic Press, 1999.
2. G. K. Boreskov, *Heterogeneous catalysis*, Nova Publishers, 2003.
3. J. M. Thomas and W. J. Thomas, *Principles and practice of heterogeneous catalysis*, John Wiley & Sons, 2014.
4. H. Liu, *Chinese J Catal*, 2014, **35**, 1619-1640.
5. J. K. Nørskov, J. Rossmeisl, A. Logadottir, L. Lindqvist, J. R. Kitchin, T. Bligaard and H. Jónsson, *J. Phys. Chem. B*, 2004, **108**, 17886-17892.
6. J. H. Holles, M. A. Switzer and R. J. Davis, *J. Catal.*, 2000, **190**, 247-260.
7. V. Polshettiwar, C. Len and A. Fihri, *Coord. Chem. Rev.*, 2009, **253**, 2599-2626.
8. A. J. Medford, A. Vojvodic, J. S. Hummelshøj, J. Voss, F. Abild-Pedersen, F. Studt, T. Bligaard, A. Nilsson and J. K. Nørskov, *J. Catal.*, 2015, **328**, 36-42.
9. Q. Fu and T. Wagner, *Surf. Sci. Rep.*, 2007, **62**, 431-498.
10. E. Gross and G. A. Somorjai, *Top. Catal.*, 2013, **56**, 1049-1058.
11. T. Mitsudome, Y. Mikami, M. Matoba, T. Mizugaki, K. Jitsukawa and K. Kaneda, *Angew. Chem. Int. Ed.*, 2012, **51**, 136-139.
12. Y. Bing, H. Liu, L. Zhang, D. Ghosh and J. Zhang, *Chem. Soc. Rev.*, 2010, **39**, 2184-2202.
13. M. Sankar, N. Dimitratos, P. J. Miedziak, P. P. Wells, C. J. Kiely and G. J. Hutchings, *Chem. Soc. Rev.*, 2012, **41**, 8099-8139.
14. D. M. Alonso, S. G. Wettstein and J. A. Dumesic, *Chem. Soc. Rev.*, 2012, **41**, 8075-8098.
15. L. Liu and A. Corma, *Chem. Rev.*, 2018, **118**, 4981-5079.
16. S. Furukawa and T. Komatsu, *ACS Catal.*, 2017, **7**, 735-765.
17. K. Ullakko, J. K. Huang, C. Kantner, R. C. OHandley and V. V. Kokorin, *Appl. Phys. Lett.*, 1996, **69**, 1966-1968.
18. J. H. Westbrook and R. L. Fleischer, *Magnetic, Electrical and Optical Properties and Applications of Intermetallic Compounds*, Wiley, 2000.
19. R. J. Cava, H. Takagi, B. Batlogg, H. W. Zandbergen, J. J. Krajewski, W. F. Peck, R. B. Vandover, R. J. Felder, T. Siegrist, K. Mizuhashi, J. O. Lee, H. Eisaki, S. A. Carter and S. Uchida, *Nature*, 1994, **367**, 146-148.
20. T. He, Q. Huang, A. P. Ramirez, Y. Wang, K. A. Regan, N. Rogado, M. A. Hayward, M. K. Haas, J. S. Slusky, K. Inumara, H. W. Zandbergen, N. P. Ong and R. J. Cava, *Nature*, 2001, **411**, 54-56.
21. K. Otsuka and X. Ren, *Intermetallics*, 1999, **7**, 511-528.
22. J. P. Oliveira, R. M. Miranda and F. M. Braz Fernandes, *Prog. Mater. Sci.*, 2017, **88**, 412-466.
23. R. Kirchheim, T. Mutschele, W. Kieninger, H. Gleiter, R. Birringer and T. D. Koble, *Mater. Sci. Eng.*, 1988, **99**, 457-462.
24. G. Sandrock, *J. Alloys Compd.*, 1999, **293-295**, 877-888.
25. T. Komatsu, M. Takasaki, K. Ozawa, S. Furukawa and A. Muramatsu, *J. Phys. Chem. C*, 2013, **117**, 10483-10491.
26. S. Furukawa, Y. Yoshida and T. Komatsu, *ACS Catal.*, 2014, **4**, 1441-1450.
27. S. Iihama, S. Furukawa and T. Komatsu, *ACS Catal.*, 2016, **6**, 742-746.
28. S. Furukawa, K. Ehara and T. Komatsu, *Catal. Sci. Technol.*, 2016, **6**, 1642-1650.
29. S. Furukawa, Y. Matsunami, I. Hamada, Y. Hashimoto, Y. Sato and T. Komatsu, *ACS Catal.*, 2018, **8**, 8177-8181.

30. S. Furukawa, G. Nishimura, T. Takayama and T. Komatsu, *Front. Chem.*, 2019, **7**.
31. M. Torimoto, S. Ogo, D. Harjowinoto, T. Higo, J. G. Seo, S. Furukawa and Y. Sekine, *Chem. Commun.*, 2019, **55**, 6693-6695.
32. H. Itahara, W. F. Simanullang, N. Takahashi, S. Kosaka and S. Furukawa, *Inorg. Chem.*, 2019, **58**, 5406-5409.
33. S. Furukawa, P. Yi, Y. Kunisada and . Shimizu, *Sci. Technol. Adv. Mat.*, 2019, **20**, 805-812.
34. T. B. Massalski, H. Okamoto, P. Subramanian and L. Kacprzak, *ASM International*, 1990, 1990, 1225-1226.
35. S. R. Bharadwaj, A. S. Kerkar, S. N. Tripathi and S. R. Dharwadkar, *J. Less-Common Met.*, 1991, **169**, 167-172.
36. P. Durussel, R. Massara and P. Feschotte, *J. Alloys Compd.*, 1994, **215**, 175-179.
37. J. A. Alonso and L. A. Girifalco, *J. Phys. Chem. Solids*, 1978, **39**, 79-87.
38. J. C. Bauer, X. Chen, Q. S. Liu, T. H. Phan and R. E. Schaak, *J. Mater. Chem.*, 2008, **18**, 275-282.
39. H. Miura, K. Endo, R. Ogawa and T. Shishido, *ACS Catal.*, 2017, **7**, 1543-1553.
40. S. Furukawa, K. Ozawa and T. Komatsu, *RSC Adv.*, 2013, **3**, 23269-23277.
41. S. Furukawa, R. Suzuki and T. Komatsu, *ACS Catal.*, 2016, **6**, 5946-5953.
42. S. Furukawa, A. Suga and T. Komatsu, *ACS Catal.*, 2015, **5**, 1214-1222.
43. T. Komatsu and S. Furukawa, *Mater Trans*, 2015, **56**, 460-467.
44. H. Knozinger, in *Stud. Surf. Sci. Catal.*, eds. B. Imelik, C. Naccache, G. Coudurier, Y. B. Taarit and J. C. Vedrine, Elsevier, 1985, vol. 20, pp. 111-125.
45. F. Mulcahy, *J. Catal.*, 1987, **106**, 210-215.
46. F. Pinna, *Catal. Today*, 1998, **41**, 129-137.
47. S. Furukawa, M. Endo and T. Komatsu, *ACS Catal.*, 2014, **4**, 3533-3542.
48. G. Saravanan, H. Abe, Y. Xu, N. Sekido, H. Hirata, S. Matsumoto, H. Yoshikawa and Y. Yamabe-Mitarai, *Langmuir*, 2010, **26**, 11446-11451.
49. H. Abe, F. Matsumoto, L. R. Alden, S. C. Warren, H. D. Abruna and F. J. DiSalvo, *J. Am. Chem. Soc.*, 2008, **130**, 5452-5458.
50. G. V. Ramesh, R. Kodyath, T. Tanabe, M. Manikandan, T. Fujita, N. Umezawa, S. Ueda, S. Ishihara, K. Ariga and H. Abe, *Acs Appl Mater Inter*, 2014, **6**, 16124-16130.
51. G. A. Somorjai and D. W. Blakely, *Nature*, 1975, **258**, 580-583.
52. J. R. Creighton and J. M. White, *Surf. Sci.*, 1983, **129**, 327-335.
53. E. Vesselli, A. Baraldi, G. Comelli, S. Lizzit and R. Rosei, *ChemPhysChem*, 2004, **5**, 1133-1140.
54. Y. Chen and D. G. Vlachos, *J. Phys. Chem. C*, 2010, **114**, 4973-4982.
55. D. Ferri, C. Mondelli, F. Krumeich and A. Baiker, *J. Phys. Chem. B*, 2006, **110**, 22982-22986.
56. D. M. Meier, A. Urakawa and A. Baiker, *J. Phys. Chem. C*, 2009, **113**, 21849-21855.
57. H. Wang, Q. Luo, W. Liu, Y. Lin, Q. Guan, X. Zheng, H. Pan, J. Zhu, Z. Sun, S. Wei, J. Yang and J. Lu, *Nat. Commun.*, 2019, **10**, 4998.
58. J. Zhu Chen, Z. Wu, X. Zhang, S. Choi, Y. Xiao, A. Varma, W. Liu, G. Zhang and J. T. Miller, *Catal. Sci. Technol.*, 2019, **9**, 1349-1356.
59. S. Zha, G. Sun, T. Wu, J. Zhao, Z.-J. Zhao and J. Gong, *Chem. Sci.*, 2018, **9**, 3925-3931.
60. Z. Wu, B. C. Bukowski, Z. Li, C. Milligan, L. Zhou, T. Ma, Y. Wu, Y. Ren, F. H. Ribeiro, W. N. Delgass, J. Greeley, G. Zhang and J. T. Miller, *J. Am. Chem. Soc.*, 2018, **140**, 14870-14877.
61. M. L. Yang, Y. A. Zhu, X. G. Zhou, Z. J. Sui and D. Chen, *ACS Catal.*, 2012, **2**, 1247-1258.
62. S. Furukawa, A. Tamura, K. Ozawa and T. Komatsu, *Appl. Catal. A: Gen.*, 2014, **469**, 300-305.
63. L. Deng, T. Shishido, K. Teramura and T. Tanaka, *Catal. Today*, 2014, **232**, 33-39.
64. J. J. H. B. Sattler, J. Ruiz-Martinez, E. Santillan-Jimenez and B. M. Weckhuysen, *Chem. Rev.*, 2014, **114**, 10613-10653.
65. T. Wang, F. Jiang, G. Liu, L. Zeng, Z.-j. Zhao and J. Gong, *AIChE J.*, 2016, **62**, 4365-4376.
66. L. Nykänen and K. Honkala, *J. Phys. Chem. C*, 2011, **115**, 9578-9586.
67. E. Nikolla, J. Schwank and S. Linic, *J. Am. Chem. Soc.*, 2009, **131**, 2747-2754.
68. S. Furukawa, K. Ehara, K. Ozawa and T. Komatsu, *Phys. Chem. Chem. Phys.*, 2014, **16**, 19828-19831.
69. C. Xu, Y. L. Tsai and B. E. Koel, *J. Phys. Chem.*, 1994, **98**, 585-593.
70. M. K. Sabbe, L. Láin, M.-F. Reyniers and G. B. Marin, *Phys. Chem. Chem. Phys.*, 2013, **15**, 12197-12214.
71. S. I. Murahashi, *Angew Chem Int Edit*, 1995, **34**, 2443-2465.
72. M. Szwarc and M. G. Evans, *Proceedings of the Royal Society of London. Series A. Mathematical and Physical Sciences*, 1949, **198**, 285-292.
73. M. Szwarc, *J. Chem. Phys.*, 1949, **17**, 431-435.

74. S. Furukawa, A. Suga and T. Komatsu, *Chem. Commun.*, 2014, **50**, 3277-3280.
75. L. Pauling, *J. Am. Chem. Soc.*, 1947, **69**, 542-553.
76. S. A. Lawrence, *Amines: synthesis, properties and applications*, Cambridge University Press, 2004.
77. K. Shimizu, N. Imaiida, K. Kon, S. M. A. H. Siddiki and A. Satsuma, *ACS Catal.*, 2013, **3**, 998-1005.
78. . Shimizu, *Catal. Sci. Technol.*, 2015, **5**, 1412-1427.
79. K. Pitchumani, A. Joy, N. Prevost and V. Ramamurthy, *Chem. Commun.*, 1997, 127-128.
80. Y. Inoue, S. Takamuku and H. Sakurai, *J. Phys. Chem.*, 1977, **81**, 7-11.
81. J. Horiuti and M. Polanyi, *T. Faraday Soc.*, 1934, **30**, 1164-1172.
82. S. Furukawa, K. Ochi, H. Luo, M. Miyazaki and T. Komatsu, *ChemCatChem*, 2015, **7**, 3472-3479.
83. S. Furukawa and T. Komatsu, *ACS Catal.*, 2016, **6**, 2121-2125.
84. *World Patent 91/00278 Pat.*, 1991.
85. R. S. Downing, P. J. Kunkeler and H. vanBekkum, *Catal. Today*, 1997, **37**, 121-136.
86. P. N. Rylander, *Catalytic Hydrogenation in Organic Synthesis*, Academic Press, New York, 1979.
87. S. Furukawa, K. Takahashi and T. Komatsu, *Chem. Sci.*, 2016, **7**, 4476-4484.
88. M. Miyazaki, S. Furukawa and T. Komatsu, *J. Am. Chem. Soc.*, 2017, **139**, 18231-18239.
89. T. Biswas and K. Schubert, *J. Less-Common Met.*, 1969, **19**, 223-243.
90. J. H. Wang, H. Chen, Z. C. Hu, M. F. Yao and Y. D. Li, *Catal. Rev.*, 2015, **57**, 79-144.
91. J. H. Holles, R. J. Davis, T. M. Murray and J. M. Howe, *J. Catal.*, 2000, **195**, 193-206.
92. W. Z. An, Q. L. Zhang, K. T. Chuang and A. R. Sanger, *Ind. Eng. Chem. Res.*, 2002, **41**, 27-31.
93. J. Shibata, M. Hashimoto, K. Shimizu, H. Yoshida, T. Hattori and A. Satsuma, *J. Phys. Chem. B*, 2004, **108**, 18327-18335.
94. A. Srinivasan and C. Depcik, *Catal. Rev.*, 2010, **52**, 462-493.
95. J. Jeon, . Kon, T. Toyao, . Shimizu and S. Furukawa, *Chem. Sci.*, 2019, **10**, 4148-4162.
96. Y. Nakaya, M. Miyazaki, S. Yamazoe, . Shimizu and S. Furukawa, *ACS Catal.*, 2020, **10**, 5163-5172.
97. R. B. Biniwale, S. Rayalu, S. Devotta and M. Ichikawa, *Int. J. Hydrogen Energy*, 2008, **33**, 360-365.
98. E. Gianotti, M. I. Taillades-Jacquín, J. Rozière and D. J. Jones, *ACS Catal.*, 2018, **8**, 4660-4680.
99. Y. Okada, E. Sasaki, E. Watanabe, S. Hyodo and H. Nishijima, *Int. J. Hydrogen Energy*, 2006, **31**, 1348-1356.
100. F. Alhumaidan, D. Cresswell and A. Garforth, *Energ. Fuel.*, 2011, **25**, 4217-4234.
101. F. Heusler, *Dtsch. Phys. Ges.*, 1903, **5**, 219.
102. T. Kojima, S. Kameoka, S. Fujii, S. Ueda and A.-P. Tsai, *Sci. Adv.*, 2018, **4**, eaat6063.
103. T. Kojima, S. Kameoka and A. Tsai, *Sci. Technol. Adv. Mat.*, 2019, **20**, 445-455.
104. T. Graf, C. Felser and S. S. Parkin, *Handbook of spintronics*, 2016, 335-364.
105. Y. Nishino, H. Kato, M. Kato and U. Mizutani, *Phys. Rev. B*, 2001, **63**, 233303.
106. A. Planes, L. Mañosa and M. Acet, *J. Phys. Condens. Matter*, 2009, **21**, 233201.
107. J. A. Hedvall and H. Rune, *Z. Phys. Chem.*, 1935, **30B**, 280-288.
108. T. Kojima, S. Kameoka and A. Tsai, *ACS omega*, 2017, **2**, 147-153.
109. T. Kojima, S. Kameoka and A. Tsai, *ACS omega*, 2019, **4**, 21666-21674.
110. V. Ponc, *Catalysis Reviews*, 1975, **11**, 41-70.
111. J. K. A. Clarke, *Chem. Rev.*, 1975, **75**, 291-305.
112. V. Ponc and G. C. Bond, *Catalysis by metals and alloys*, Elsevier, 1995.
113. V. Ponc, *Appl. Catal. A: Gen.*, 2001, **222**, 31-45.
114. K. Kusada, H. Kobayashi, R. Ikeda, Y. Kubota, M. Takata, S. Toh, T. Yamamoto, S. Matsumura, N. Sumi, K. Sato, K. Nagaoka and H. Kitagawa, *J. Am. Chem. Soc.*, 2014, **136**, 1864-1871.
115. K. Sato, H. Tomonaga, T. Yamamoto, S. Matsumura, N. D. B. Zulkifli, T. Ishimoto, M. Koyama, K. Kusada, H. Kobayashi, H. Kitagawa and K. Nagaoka, *Sci Rep-Uk*, 2016, **6**, 28265.
116. M. S. Kutubi, K. Sato, K. Wada, T. Yamamoto, S. Matsumura, K. Kusada, H. Kobayashi, H. Kitagawa and K. Nagaoka, *ChemCatChem*, 2015, **7**, 3887-3894.
117. A. A. Vedyagin, R. M. Kenzhin, M. Y. Tashlanov, E. A. Alikin, V. O. Stoyanovskii, P. E. Plyusnin, Y. V. Shubin, I. V. Mishakov, M. Y. Smirnov, A. V. Kalinkin and V. I. Bukhtiyarov, *Top. Catal.*, 2020, **63**, 152-165.
118. A. A. Vedyagin, E. A. Alikin, R. M. Kenzhin, M. Y. Tashlanov, V. O. Stoyanovskii, P. E. Plyusnin, Y. V. Shubin and I. V. Mishakov, *Reaction Kinetics, Mechanisms and Catalysis*, 2020, **129**, 117-133.
119. A. A. Vedyagin, V. O. Stoyanovskii, R. M. Kenzhin, E. M. Slavinskaya, P. E. Plyusnin and Y. V. Shubin, *Reaction Kinetics, Mechanisms and Catalysis*, 2019, **127**, 137-148.
120. A. A. Vedyagin, Y. V. Shubin, R. M. Kenzhin, P. E. Plyusnin, V. O. Stoyanovskii and A. M. Volodin, *Top. Catal.*, 2019, **62**, 305-314.

121. A. A. Vedyagin, R. M. Kenzhin, M. Y. Tashlanov, V. O. Stoyanovskii, P. E. Plyusnin, Y. V. Shubin, I. V. Mishakov, A. V. Kalinkin, M. Y. Smirnov and V. I. Bukhtiyarov, *Emission Control Science and Technology*, 2019, **5**, 363-377.
122. P. E. Plyusnin, E. M. Slavinskaya, R. M. Kenzhin, A. K. Kirilovich, E. V. Makotchenko, O. A. Stonkus, Y. V. Shubin and A. A. Vedyagin, *Reaction Kinetics, Mechanisms and Catalysis*, 2019, **127**, 69-83.
123. G. A. Kostin, P. E. Plyusnin, E. Y. Filatov, N. V. Kuratieva, A. A. Vedyagin and D. B. Kal'nyi, *Polyhedron*, 2019, **159**, 217-225.
124. A. A. Vedyagin, V. O. Stoyanovskii, P. E. Plyusnin, Y. V. Shubin, E. M. Slavinskaya and I. V. Mishakov, *J. Alloys Compd.*, 2018, **749**, 155-162.
125. A. A. Vedyagin, P. E. Plyusnin, A. A. Rybinskaya, Y. V. Shubin, I. V. Mishakov and S. V. Korenev, *Mater. Res. Bull.*, 2018, **102**, 196-202.
126. Y. V. Shubin, A. A. Vedyagin, P. E. Plyusnin, A. K. Kirilovich, R. M. Kenzhin, V. O. Stoyanovskii and S. V. Korenev, *J. Alloys Compd.*, 2018, **740**, 935-940.
127. A. A. Vedyagin, A. M. Volodin, R. M. Kenzhin, V. O. Stoyanovskii, Y. V. Shubin, P. E. Plyusnin and I. V. Mishakov, *Catal. Today*, 2017, **293-294**, 73-81.
128. Y. V. Shubin, P. E. Plyusnin and S. V. Korenev, *J. Alloys Compd.*, 2015, **622**, 1055-1060.
129. A. A. Vedyagin, A. M. Volodin, V. O. Stoyanovskii, R. M. Kenzhin, E. M. Slavinskaya, I. V. Mishakov, P. E. Plyusnin and Y. V. Shubin, *Catal. Today*, 2014, **238**, 80-86.
130. A. A. Vedyagin, M. S. Gavrilov, A. M. Volodin, V. O. Stoyanovskii, E. M. Slavinskaya, I. V. Mishakov and Y. V. Shubin, *Top. Catal.*, 2013, **56**, 1008-1014.
131. A. A. Rybinskaya, P. E. Plyusnin, E. A. Bykova, S. A. Gromilov, Y. V. Shubin and S. V. Korenev, *J. Struct. Chem.*, 2012, **53**, 527-533.
132. Y. V. Shubin, S. V. Korenev and M. R. Sharafutdinov, *Russ. Chem. Bull.*, 2006, **55**, 1109-1113.
133. S. Furukawa, M. Ieda and . Shimizu, *ACS Catal.*, 2019, **9**, 5096-5103.
134. Y. Wang, S. Furukawa, S. Song, Q. He, H. Asakura and N. Yan, *Angew. Chem. Int. Ed.*, 2020, **59**, 2289-2293.
135. Y. Wang, S. Furukawa and N. Yan, *ACS Catal.*, 2019, **9**, 6681-6691.
136. M. T. Greiner, T. E. Jones, S. Beeg, L. Zwiener, M. Scherzer, F. Girgsdies, S. Piccinin, M. Armbrüster, A. Knop-Gericke and R. Schlögl, *Nat. Chem.*, 2018, **10**, 1008-1015.
137. F. R. Lucci, J. Liu, M. D. Marcinkowski, M. Yang, L. F. Allard, M. Flytzani-Stephanopoulos and E. C. H. Sykes, *Nat. Commun.*, 2015, **6**, 8550.
138. J. Liu, F. R. Lucci, M. Yang, S. Lee, M. D. Marcinkowski, A. J. Therrien, C. T. Williams, E. C. H. Sykes and M. Flytzani-Stephanopoulos, *J. Am. Chem. Soc.*, 2016, **138**, 6396-6399.
139. M. D. Marcinkowski, M. T. Darby, J. Liu, J. M. Wimble, F. R. Lucci, S. Lee, A. Michaelides, M. Flytzani-Stephanopoulos, M. Stamatakis and E. C. H. Sykes, *Nat. Chem.*, 2018, **10**, 325-332.
140. M. B. Boucher, B. Zugic, G. Cladaras, J. Kammert, M. D. Marcinkowski, T. J. Lawton, E. C. H. Sykes and M. Flytzani-Stephanopoulos, *Phys. Chem. Chem. Phys.*, 2013, **15**, 12187-12196.
141. G. X. Pei, X. Y. Liu, A. Wang, A. F. Lee, M. A. Isaacs, L. Li, X. Pan, X. Yang, X. Wang, Z. Tai, K. Wilson and T. Zhang, *ACS Catal.*, 2015, **5**, 3717-3725.
142. F. R. Lucci, M. T. Darby, M. F. G. Mattera, C. J. Ivimey, A. J. Therrien, A. Michaelides, M. Stamatakis and E. C. H. Sykes, *The Journal of Physical Chemistry Letters*, 2016, **7**, 480-485.
143. J. Liu, J. Shan, F. R. Lucci, S. Cao, E. C. H. Sykes and M. Flytzani-Stephanopoulos, *Catal. Sci. Technol.*, 2017, **7**, 4276-4284.
144. Z.-T. Wang, M. T. Darby, A. J. Therrien, M. El-Soda, A. Michaelides, M. Stamatakis and E. C. H. Sykes, *J. Phys. Chem. C*, 2016, **120**, 13574-13580.
145. F. Xing, J. Jeon, T. Toyao, . Shimizu and S. Furukawa, *Chem. Sci.*, 2019, **10**, 8292-8298.
146. B. S. Murty, J.-W. Yeh, S. Ranganathan and P. Bhattacharjee, *High-entropy alloys*, Elsevier, 2019.
147. Y. Yao, Z. Huang, P. Xie, S. D. Lacey, R. J. Jacob, H. Xie, F. Chen, A. Nie, T. Pu and M. Rehwoldt, *Science*, 2018, **359**, 1489-1494.
148. P. Xie, Y. Yao, Z. Huang, Z. Liu, J. Zhang, T. Li, G. Wang, R. Shahbazian-Yassar, L. Hu and C. Wang, *Nat. Commun.*, 2019, **10**, 1-12.
149. M. Friedrich, D. Teschner, A. Knop-Gericke and M. Armbrüster, *J. Phys. Chem. C*, 2012, **116**, 14930-14935.
150. S. Furukawa, G. Nishimura and T. Komatsu, *J. Jpn. Petrol. Inst.*, 2016, **59**, 160-163.
151. V. R. Stamenkovic, B. S. Mun, M. Arenz, K. J. J. Mayrhofer, C. A. Lucas, G. Wang, P. N. Ross and N. M. Markovic, *Nat. Mater.*, 2007, **6**, 241-247.

152. C. Wang, M. Chi, D. Li, D. Strmcnik, D. van der Vliet, G. Wang, V. Komanicky, K.-C. Chang, A. P. Paulikas, D. Tripkovic, J. Pearson, K. L. More, N. M. Markovic and V. R. Stamenkovic, *J. Am. Chem. Soc.*, 2011, **133**, 14396-14403.
153. C. Cui, L. Gan, M. Heggen, S. Rudi and P. Strasser, *Nat. Mater.*, 2013, **12**, 765-771.
154. M. Miyazaki, S. Furukawa, T. Takayama, S. Yamazoe and T. Komatsu, *ACS Applied Nano Materials*, 2019, **2**, 3307-3314.
155. Y. Nakaya, J. Hirayama, S. Yamazoe, K. Shimizu and S. Furukawa, *Nat. Commun.*, 2020, **11**, 2838.
156. J. Freel, W. J. M. Pieters and R. B. Anderson, *J. Catal.*, 1969, **14**, 247-256.
157. H. Hu, F. Xie, Y. Pei, M. Qiao, S. Yan, H. He, K. Fan, H. Li, B. Zong and X. Zhang, *J. Catal.*, 2006, **237**, 143-151.
158. H. Hu, M. Qiao, S. Wang, K. Fan, H. Li, B. Zong and X. Zhang, *J. Catal.*, 2004, **221**, 612-618.
159. L.-J. Zhu, P.-J. Guo, X.-W. Chu, S.-R. Yan, M.-H. Qiao, K.-N. Fan, X.-X. Zhang and B.-N. Zong, *Green Chem.*, 2008, **10**, 1323-1330.
160. K. Xu, B. Sun, J. Lin, W. Wen, Y. Pei, S. Yan, M. Qiao, X. Zhang and B. Zong, *Nat. Commun.*, 2014, **5**, 5783.
161. T. Yamada, T. Kojima, E. Abe, S. Kameoka, Y. Murakami, P. Gille and A. P. Tsai, *J. Am. Chem. Soc.*, 2018, **140**, 3838-3841.
162. S. Kameoka, S. Wakabayashi, E. Abe and A. P. Tsai, *Catal. Lett.*, 2016, **146**, 1309-1316.
163. T. Fujita, X. Peng, A. Yamaguchi, Y. Cho, Y. Zhang, K. Higuchi, Y. Yamamoto, T. Tokunaga, S. Arai, M. Miyauchi and H. Abe, *ACS Omega*, 2018, **3**, 16651-16657.
164. S. Furukawa, A. Tsuchiya, Y. Kojima, M. Endo and T. Komatsu, *Chem. Lett.*, 2016, **45**, 158-160.
165. W. F. Simanullang, H. Itahara, N. Takahashi, S. Kosaka, K. Shimizu and S. Furukawa, *Chem. Commun.*, 2019, **55**, 13999-14002.
166. S. Shoji, X. Peng, T. Imai, P. S. Murphin Kumar, K. Higuchi, Y. Yamamoto, T. Tokunaga, S. Arai, S. Ueda, A. Hashimoto, N. Tsubaki, M. Miyauchi, T. Fujita and H. Abe, *Chem. Sci.*, 2019, **10**, 3701-3705.
167. T. Tanabe, T. Imai, T. Tokunaga, S. Arai, Y. Yamamoto, S. Ueda, G. V. Ramesh, S. Nagao, H. Hirata, S. Matsumoto, T. Fujita and H. Abe, *Chem. Sci.*, 2017, **8**, 3374-3378.



An overview of a variety of advanced alloy materials for catalytic use is provided.